

Microskeletal stiffness promotes aortic aneurysm by sustaining pathological vascular smooth muscle cell mechanosensation via Piezo1

Weiyi Qian

Department of Mechanical and Aerospace Engineering, New York University, Brooklyn, NY, USA;

Tarik Hadi

Division of Vascular and Endovascular Surgery, Department of Surgery, New York University Langone Health, New York, US

Xiao Ma

Department of Biomedical Engineering, New York University, Brooklyn, NY, USA;

Michele Silvestro

Division of Vascular and Endovascular Surgery, Department of Surgery, New York University Langone Health, New York, USA.

Cristobal Rivera

Division of Vascular and Endovascular Surgery, Department of Surgery, New York University Langone Health, New York, USA.

Apratim Bajpai

Department of Mechanical and Aerospace Engineering, New York University, Brooklyn, NY, USA;

Zijing Zhang

Department of Mechanical and Aerospace Engineering, New York University, Brooklyn, NY, USA;

Hengdong Qu

Division of Vascular and Endovascular Surgery, Department of Surgery, New York University Langone Health, New York, USA.

Annanina Corsica

Division of Vascular and Endovascular Surgery, Department of Surgery, New York University Langone Health, New York, USA.

Bradley Miscovich

Division of Vascular and Endovascular Surgery, Department of Surgery, New York University Langone Health, New York, USA.

Berk Aykut

S. Arthur Localio Laboratory, Department of Surgery, New York University Langone Health, New York, USA.

George Miller

S. Arthur Localio Laboratory, Department of Surgery, New York University Langone Health, New York, USA.

Bhama Ramkhelawon (✉ Bhama.Ramkhelawon@nyulangone.org)

Division of Vascular and Endovascular Surgery, Department of Surgery, New York University Langone Health, New York, USA.

Weiqiang Chen (✉ wchen@nyu.edu)

Department of Mechanical and Aerospace Engineering, New York University, Brooklyn, NY, USA;
<https://orcid.org/0000-0002-9469-8328>

Article

Keywords: abdominal aortic aneurysms, vascular smooth muscle cells, mechanical stress resonance, Piezo1, microskelatal stiffnesss

Posted Date: June 26th, 2020

DOI: <https://doi.org/10.21203/rs.3.rs-36390/v1>

License:  This work is licensed under a Creative Commons Attribution 4.0 International License.

[Read Full License](#)

Version of Record: A version of this preprint was published at Nature Communications on January 26th, 2022. See the published version at <https://doi.org/10.1038/s41467-021-27874-5>.

Microskeletal stiffness promotes aortic aneurysm by sustaining pathological vascular smooth muscle cell mechanosensation via Piezo1

Weiyi Qian^{1†}, Tarik Hadi^{2†}, Xiao Ma³, Michele Silvestro², Cristobal F. Rivera², Apratim Bajpai¹, Zijing Zhang¹, Hengdong Qu², Annanina Corsica², Bradley Miscovich², Berk Aykut⁴, George Miller^{4,5}, Bhama Ramkhelawon^{2,5*}, Weiqiang Chen^{1,3*}

¹Department of Mechanical and Aerospace Engineering, New York University, Brooklyn, NY, USA;

²Division of Vascular and Endovascular Surgery, Department of Surgery, New York University Langone Health, New York, USA.

³Department of Biomedical Engineering, New York University, Brooklyn, NY, USA;

⁴S. Arthur Localio Laboratory, Department of Surgery, New York University Langone Health, New York, USA.

⁵Department of Cell Biology, New York University Langone Health, New York, USA.

† These authors contributed equally to this work

* These authors contributed equally to this work

*Correspondence should be addressed to BR (bhama.ramkhelawon@nyumc.org) and WC (wchen@nyu.edu).

ABSTRACT

Mechanical overload of the vascular wall is a pathological hallmark of life-threatening abdominal aortic aneurysms (AAA). However, how this mechanical stress resonates at the unicellular level of vascular smooth muscle cells (VSMC) in AAA is undefined. Here, we combined novel ultrasound tweezers-based micromechanical system and single-cell RNA sequencing to map defective mechano-phenotype signature of VSMC niched in AAA. VSMC gradually adopted a mechanically solid-like state by upregulating cytoskeleton (CSK) crosslinker, α -actinin2, which stiffened VSMC cell membrane thereby directly powering the activity of mechano-sensory ion channel Piezo1 during AAA development. Theoretical modelling predicted that in AAA, such CSK alterations fueled cell membrane tension thereby blocking physiological mechanoallostatic responses of VSMC. Single-cell mechanical measurements and frequency spectrum analysis validated the mechanosensation deficiency in VSMC during AAA development. Our findings demonstrate that deviations of mechanosensation behaviors of VSMC is detrimental for AAA and identifies Piezo1 as a novel target to curb AAA onset.

INTRODUCTION

Abdominal aortic aneurysm (AAA) is a complex and lethal vascular disease with high incidence worldwide^{1,2}. The early stages of the disease onset are characterized by a mechanical deformation of the aorta that reflects vascular inflammation and intricate damage to the extracellular matrix (ECM)^{3,4}. Despite cumulative research efforts that unmasked pathological signals that contribute to AAA development, the mechanisms underlying AAA progression and the factors that further feed ECM deformation are poorly understood. Vascular smooth muscle cells (VSMC) are key regulators of ECM and their contractile function and strategic location within the vascular wall suggests that they could serve as a spatiotemporal mechanical rheostats. However, there is a paucity of evidence that precisely mapped mechanical stress and captured pathological mechanosensation of VSMC within the misshaped silhouette in AAA.

Impairment of VSMC mechanosensation due to the hereditary mutations of gene controlling VSMC cytoskeleton (CSK) contractile function has been implied for the rise of aneurysm in the thoracic compartment⁵. Acting as critical rheostats, CSK machinery is dynamic allowing cells to adapt to mechanical perturbations in the microenvironment⁶. Evidence suggests that abnormal acclimation of VSMC to biomechanical perturbations, such as increased circumferential stress in hypertension can impact VSMC signaling and stimulate AAA development⁷⁻⁹. However, insights into the change of VSMC CSK integrity and the resulting pathological mechanosensation in AAA have not been explored.

CSK integrity plays a vital role in mediating downstream mechanotransduction responses through mechanosensitive ion channels¹⁰⁻¹². Piezo1, is one of such mechanical sensors positioned at the cell membrane of cells that licenses the entry of ions including Ca²⁺ upon its activation driven by stiffened force energy¹³⁻¹⁷. Furthermore, Piezo1 channels have been shown to act as critical regulators of the vascular development^{18,19} and hypertension-dependent arterial remodeling²⁰. However, the behavior of Piezo1 channel in VSMC within a mechanically compromised AAA microenvironment is undefined. In addition to the mechanical stimuli, molecular signals concentrate within the AAA sac and might impact mechanotransduction signals in VSMC. We have previously shown that neuronal guidance protein Netrin-1 was released from transmural macrophages and promoted AAA by sustaining downstream Ca²⁺ signals necessary to stimulate matrix degrading metalloproteinase MMP3 in VSMC²¹⁻²³. Nevertheless, whether the pathological proteolytic switch of VSMC triggered by Netrin-1 in AAA could be driven by mechanosensitive microskeletal alterations via Piezo1 is undefined.

Here, we show the transition of VSMC to a more solid-like state during AAA development driven by elevated CSK crosslinking protein, α -actinin2. Loss-of-function of Netrin-1 prevented AAA development as previously shown²² and relieved arterial tension by inhibiting α -actinin2 expression. Using a sophisticated ultrasound tweezers-based micromechanical system, we experimentally and theoretically captured dynamic stiffness and impaired mechanosensing profiles of VSMC niched in AAA. Stiffened VSMC CSK

powered mechanical energy necessary to induce and activate mechanoresponsive Ca^{2+} channel Piezo1. Antagonizing Piezo1 refrained matrix degradation and prevented the development of AAA. Our study reveals how pathology can arise from defective mechanosenation due to mechanical transition of cellular material properties.

RESULTS

CSK crosslinking is increased in VSMC in stiffened aortic tissue in AAA.

To determine the transition of mechanical properties of VSMC in AAA, we measured the level of stiffness in the vascular wall in experimental AAA. We first compared aortic stiffness of diseased and control murine aortas captured by pulse wave velocity (PWV) weekly (Figure 1a) using the diameter-velocity method²⁴. Aortic PWV revealed that the vessel wall stiffness was incrementally increased in AAA compared to controls (Figure 1b), consistent with previous report²⁵. An increase in both peak velocity value (Figure 1b, red arrow) and amplitude of the wave (Figure 1b, blue curve) were observed in the AAA sac compared to that from equivalent pararenal region of non-diseased aortas. These results demonstrated that local stiffness of the vessel wall is increased in AAA.

To delve into the molecular mechanisms underlying the accrual of tension observed in AAA progression, we compared mechanosensitive signatures of healthy and aneurysmal abdominal aortas by single-cell RNA-sequencing. Using t-distributed stochastic neighbor embedding (t-SNE) nonlinear dimension-reduction method, six distinct aortic sub-populations were identified as per their genetic distribution patterns (Figure 1c). We focused on the analysis of VSMC clusters which were determined based on high expression level of markers including α -actin2 (Acta2), Myosin heavy chain 11 (Myh11) and Myosin regulatory light chain 9 (Myl9). Utilizing an adjusted nominal P value of ≤ 0.05 , we generated a heatmap representation that captured a large range of transcriptome differential expression patterns in VSMC niched in AAA compared to controls (Supplementary Figure 1). Gene Set Enrichment Analysis (GSEA) using the Database for Annotation, Visualization and Integrated Discovery (DAVID) software revealed that several signaling pathways were altered in VSMC from AAA. Notably, genes involved in vascular remodeling (MMP2 and MMP3) as well as regulation of actin CSK were the most significantly enriched networks in VSMC from AAA (Figure 1d). Analysis of the transcripts comprising CSK network demonstrated that the gene encoding for α -actinin isoform 2 (Actn2), a key regulator of actin filaments crosslinking^{26,27}, was the most significantly upregulated in VSMC from AAA (Figure 1e). Immunofluorescence staining using anti- α -actinin2 and anti- α -smooth muscle actin antibodies revealed that the protein expression of α -actinin2 was elevated and colocalized in VSMC in AAA (Figure 1f). Notably, analysis of images captured from human AAA and control sections demonstrated a similar pattern of expression characterized by an increased level of α -actinin2 within VSMC in AAA (Figure 1g). Atomic force microscopy (AFM) nanoindentation assays revealed a range of intra-aortic force magnitudes which peaked in nanoscale regions enriched in α -actinin2 indicative of stiffened territories within the tissue (Figure 1h). These

results suggested that α -actinin2 is a major integrator of stiffened force in VSMC thereby reinforcing mechanical strength in the vascular wall during AAA.

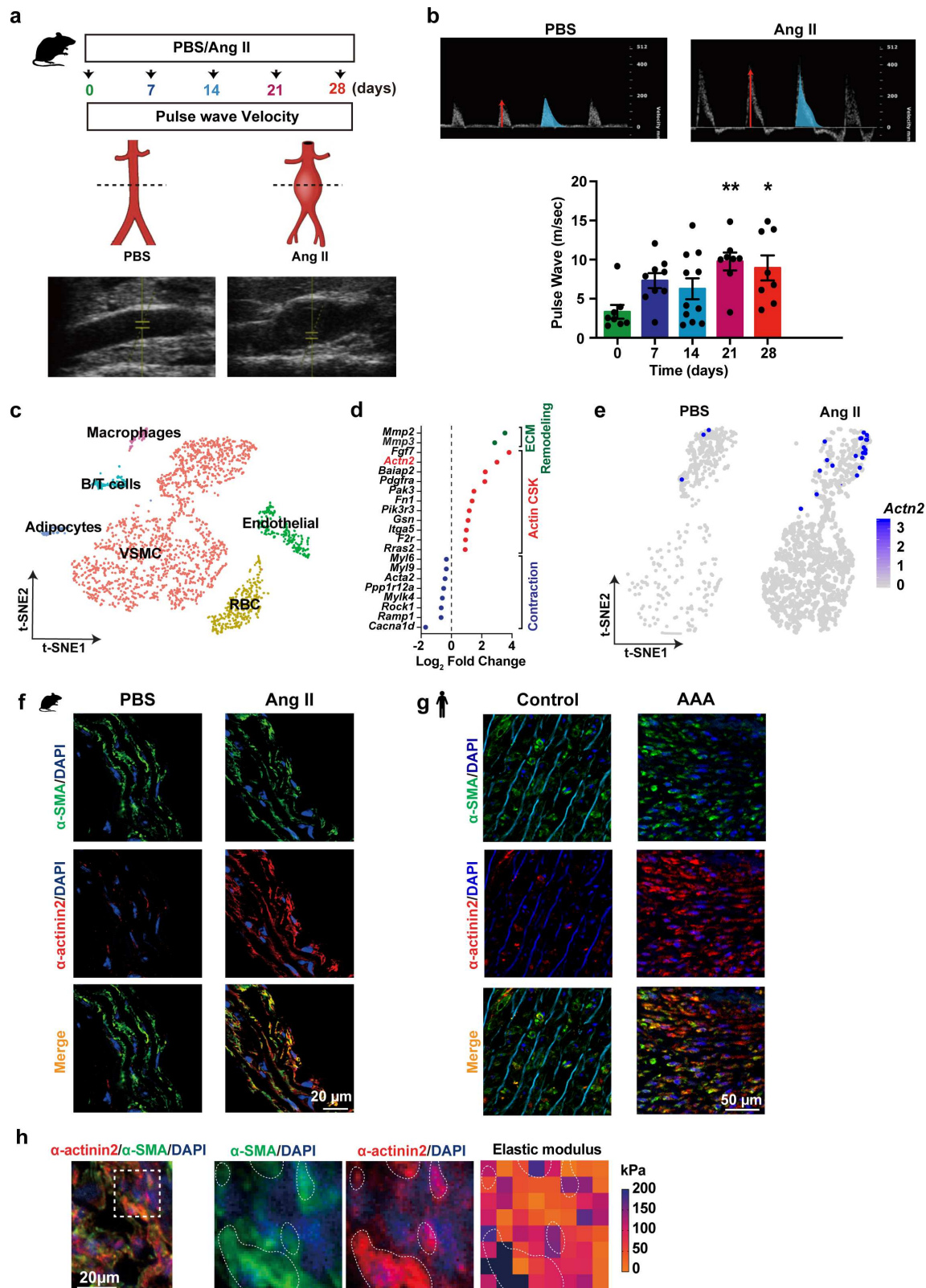


Figure 1. (a) Schematic representation of experimental protocol of PBS (control) or Angiotensin II (Ang II) perfusion in mice with timeline of pulse wave velocity (PWV) measurements. (b) Representative images of ultrasonography 2D scan images peak systolic velocity (red arrow), global pulse wave curve (blue curve) and PWV quantification of mice exposed to Ang II for days as indicated. (c) *t*-distributed stochastic neighbor embedding (*t*-SNE) plot of single-cell RNA-sequencing of mice aortas (n = 3 each). Cell clusters are color coded as indicated. Vascular smooth muscle cells, VSMC; red blood cells, RBC. (d) Selection of transcript expression in VSMC from AAA compared to control; genes are clustered according to biological process. (e) T-SNE distribution of *Actn2* mRNA (log₂ expression) within the clusters and across conditions, as indicated. Immunofluorescence (IF) staining of α -actinin2 (red) and α -SMA (green) in aortas of Ang II or PBS-infused mice (f) and in AAA or healthy human aortas (g). (h) Representative IF merged image of α -SMA (green) and α -actinin2 (red) in aortic section of mice perfused with Ang II (left panel). Dashed box shows magnified area of atomic force microscopy (AFM) measurement and heatmap representation of elastic modulus captured by AFM (right panel, dotted lines demarcate regions enriched in α -actinin2 with maximum force). Nuclei in DAPI (blue) shown in all IF images. * P< 0.05, ** P<0.01. Data are presented as average \pm s.e.m.; P values were calculated using one-way ANOVA (b).

Micromechanical system maps defective mechanosensation of VSMC in AAA

To evaluate how the elevation of α -actinin2 in VSMC in aneurysmal milieu affects VSMC contractile function and mechanosensation, we engineered a sophisticated single-cell micromechanical system (Figure 2a, b) consisting of ultrasound tweezers and a micropillar-based mechanical sensor allowing measurements of baseline CSK tension as well as the response to ultrasound stimulus mediated by a microbubble system²⁸⁻³⁰. Electron microscopy captured images of VSMC adhering to micropillars (Figure 2c) revealing displacement of pillars at the circumference of VSMC. This coincided with images of displaced micropillars at the periphery of VSMC (Supplementary Figure 2a-d). For the ultrasound tweezers, we applied a 10-second, 1 Hz, ~100 pN transient and local force to single VSMC through an RGD-integrin bonded lipid-encapsulated microbubble on the cell membrane under ultrasound excitation (Figure 2d). Activation of the system by ultrasound pulses generated acoustic radiation force on the microbubbles, causing its displacement (Figure 2e, Supplementary Figure 2e) and therefore, allowing the application of a controllable mechanical stress on cells through a microbubble-integrin-actin CSK interaction as shown in the inset in figure 2b. We first tested whether ultrasound-induced transient mechanical stimulation could activate Ca²⁺ ion influx in VSMC isolated from mouse abdominal aortas. Immediately after the application of ultrasound stimulation, Ca²⁺ influx, assessed by fluo-4 calcium sensor probe, was clearly detected in VSMC (Figure 2f), suggesting that the microbubble-integrin-actin CSK linkage can serve as a mechanosensory signal to trigger intracellular mechanical transduction.

We then applied our integrated single-cell micromechanical system to capture

mechanosensation response of primary VSMC isolated from control or aneurysmal microenvironments. Within 30 mins after the onset of the 10-second ultrasound stimulation, both healthy and AAA VSMC CSK tension exhibited a biphasic dynamic, in which the single-cell level CSK tension increased continuously within the reinforcement period (0-5 min) and restored to their ground state in the relaxation period (5-30 min) as depicted by force map of individual cells and quantification of normalized force over 30 minutes (Figure 2g). No significant change was observed in unstimulated cells (Supplementary Figure 3). In-depth characterization of temporal CSK tension during instantaneous mechanosensation revealed that while VSMC from AAA milieu generally have a higher CSK tension at the ground state, they exhibited a compromised ability to generate mechanoallostatic force compared to control (Figure 2h).

To further delve into the intrinsic alterations of CSK associated with the differential mechanosensation of VSMC in AAA, we performed an instantaneous frequency spectrum analysis, due to its profound sensitivity in capturing intrinsic CSK characteristics and mechanosensation based on Hilbert-Huang transform (HHT)³¹. Decomposition of the subcellular CSK tension by HHT (Supplementary Figure 4a) generated distinct intrinsic mode functions (IMFs) at a unicellular level of VSMC before and after ultrasound stimulus (Supplementary Figure 4b, c). We observed intrinsic blue shift of VSMC CSK tension instantaneous frequency spectra after ultrasound stimulation (Supplementary Figure 4d), indicating that the CSK tension frequency spectrum encodes the wiring of the molecular circuitry that regulates VSMC mechanosensation. When comparing the instantaneous frequency spectra for healthy and AAA VSMC, we found that VSMC from AAA displayed an intrinsic blunt in mechanosensitivity as demonstrated by a decrease in response frequency (Figure 2i). Such changes of VSMC mechanosensation was further featured by generating a combined frequency-amplitude energy heatmap to reflect the decrease of energy consumed by VSMC in pathological mechanosensation in AAA (Figure 2j). Taken together, we demonstrate that single cell mechanosensation characterization is a reliable technique capable of capturing CSK-mediated mechanosensitive imprints of VSMC niched in AAA milieu.

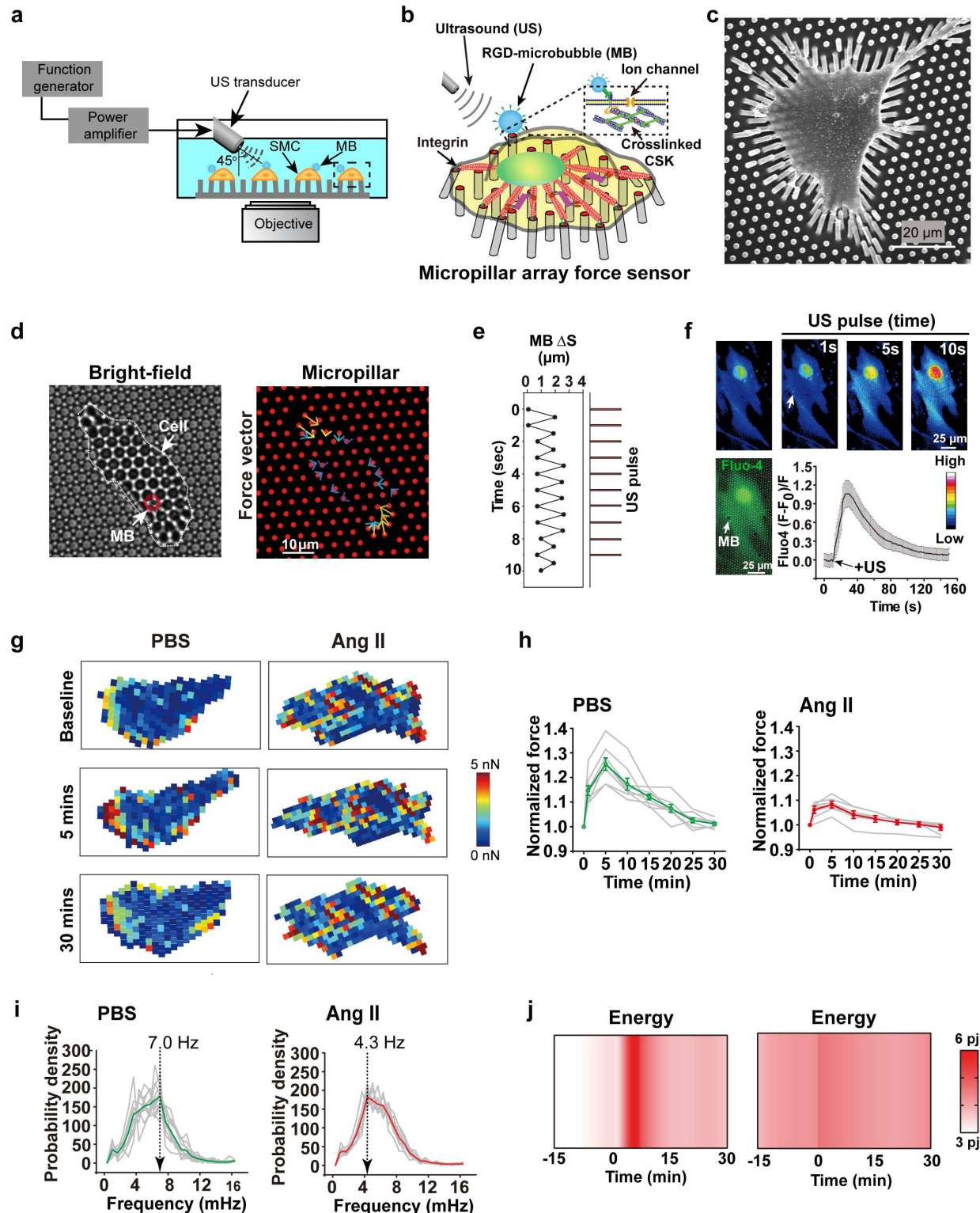


Figure 2. (a) A schematic showing the integrated micromechanical system by using ultrasound (US) excitation of microbubbles (MB) attached via RGD-integrin binding to the membrane of VSMC seeded on the PDMS micropillar array. (b) Diagram illustrating micropillar-based mechanical force sensor to probe and ultrasound tweezer system in

single cell. (c) Representative scanning electron microscopy (SEM) image showing single VSMC seeded on PDMS micropillars. (d) Representative microscopy images of bright field (left panel) and red channel showing micropillars (right panel). VSMC is delineated by dotted line, microbubble (MB) is shown by white arrow, blue and yellow arrows represent force vector. (e) Relative microbubble movement in response to 10-second, 1 Hz transient ultrasound stimulation. (f) Representative microscopy images of green channel showing Fluo-4 Ca²⁺ probe and quantification of Ca²⁺ influx in response to US stimulation. n=13. Data are presented as mean value ± s.e.m. (g) Representative heatmap representation of baseline micropillar traction force or in response to US stimulation (5 and 30 minutes) of single VSMC isolated from PBS or Ang II treated mice. Normalized global traction force (h) and mean frequency (i) of VSMC response to ultrasound stimulation. n≥8. Data are presented as mean value ± s.e.m (green and red curves), individual values are shown in grey. (j) Representative temporal heatmap of consumed energy in VSMC isolated from PBS or Ang II treated mice in response to ultrasound stimulation.

VSMC microskeletal force and mechanosensation are temporally impaired during AAA

We next delineated at which time point during AAA disease progression, modeled by continuous angiotensin II (Ang II) treatment in mice, does VSMC endure a shift in CSK mechanosensation. VSMC were isolated from the abdominal aorta following 7, 14, 21 and 28 days of Ang II infusion (Figure 3a) which allowed the study of mechanosensation behaviors of VSMC from early, mid and advanced stages of AAA development. We observed a progressive increase of ground state CSK tension in VSMC over the experimental course of AAA development (Figure 3b). Interestingly, instantaneous mechanosensation characterized by the dynamic force generation of VSMC showed an opposite trend compared to their mechanobiological ground states (Figure 3c, d). By mapping the VSMC mechanobiological responses, we discovered a negative correlation between VSMC instantaneous mechanosensation and AAA development (Figure 3e). Specifically, VSMC isolated from mice with advanced AAA displayed significant inability of generating contractile force within the reinforcement period (0-5 min) upon stimulation with a localized stress. By implementing the spatiotemporal sampling and frequency spectrum analysis of global and local CSK tension during mechanosensation, we revealed significant redshift in the frequency spectra of VSMC instantaneous contraction during AAA development (Figure 3f). Deriving response time from the reciprocal of IMF central frequency³² in instantaneous mechanosensation further indicated a prolonged response of VSMC mechanosensation as AAA progress (Figure 3g). Accordingly, response time was increased while maximum force generation was decreased following stimulation (Figure 3h). Thus, our results indicate that while basal force of VSMC is increased in AAA, their ability to resonate to mechanical stimuli and generate efficient mechanosensitivity is mitigated.

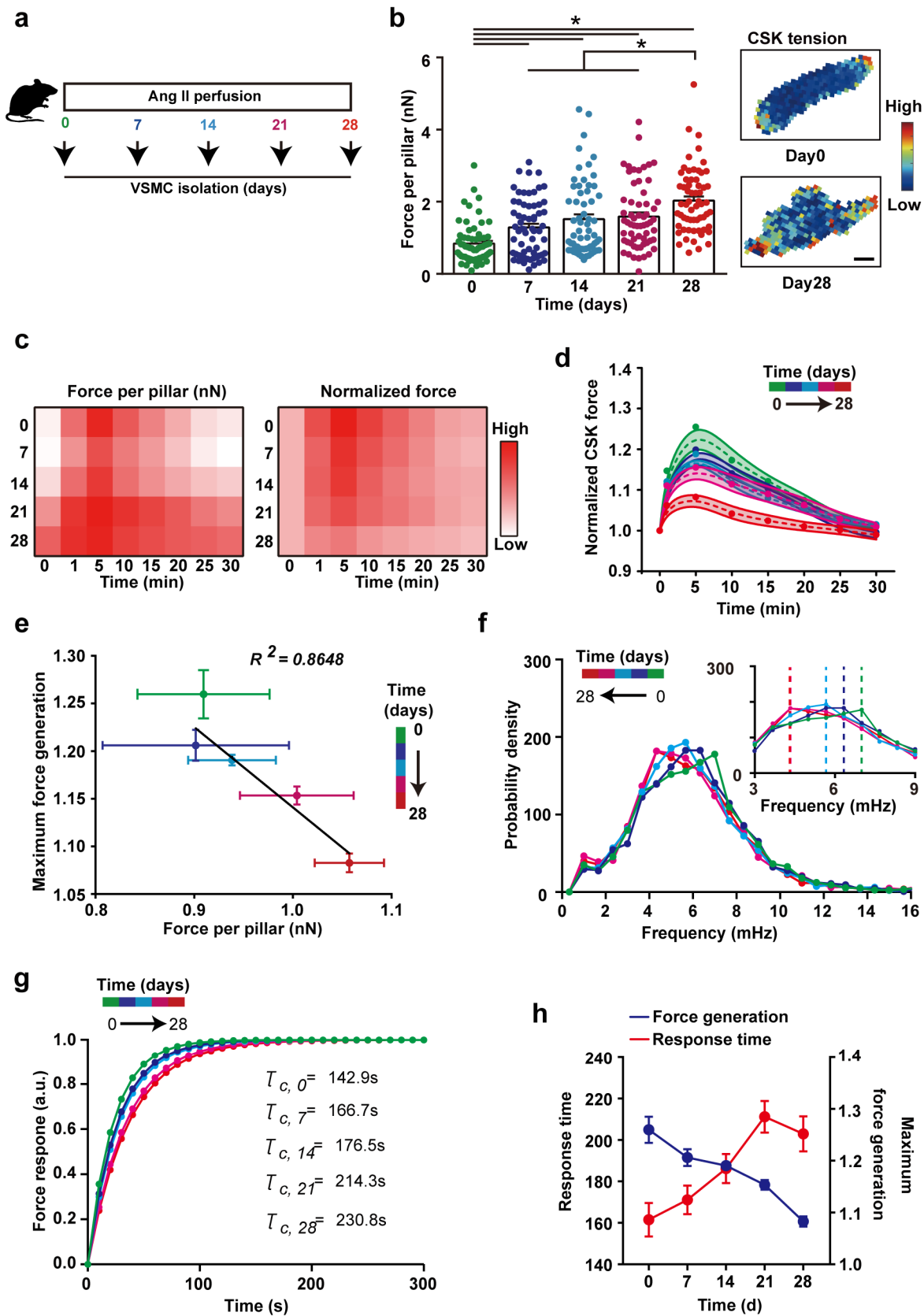


Figure 3. (a) Schematic of experimental protocol for Ang II perfusion in mice and isolation (b) Quantification and representative heatmaps (day 0 and 28) of mean basal tension per pillar in VSMC extracted from aorta at timepoint indicated. n≥60. Data are presented as mean value ± s.e.m. Each dot represents single cell quantification. (c) Heat maps showing temporal evolution of mean force per pillar (left) and mean normalized tension (right) of AAA VSMC over time during instantaneous mechanosensation. (d) Temporal profiles for each time point (color coded as in a) of normalized CSK tension per pillar of VSMC in response to 10-sec mechanical stress. n=8, data are presented as mean value ± s.e.m. Correlation analysis of VSMC progressive basal CSK tension in AAA and maximum force generation in instantaneous mechanosensation (e). Instantaneous frequency distribution (f), characteristic curves for deriving response time of instantaneous mechanosensation (g) and force generation ability (blue) and response time (red) (h) of VSMC extracted from aorta exposed to Ang II at time points as indicated by color code. n=8, data are presented as mean value ± s.e.m.

Defective CSK-mediated mechanosensation of VSMC can be predicted in AAA

In light of our experimental findings, we developed a predictive biophysical kinetics model that incorporated three key actomyosin CSK events: CSK viscoelastic deformation and relaxation, actomyosin activation and contraction, and mechanical-induced Ca^{2+} influx (Figure 4a). We adopted the Kelvin-Voigt-Myosin (KVM) model³³ to specifically study how pathological increases of α -actinin2 in VSMC can lead to different mechanosensation dynamics (Figure 4b) in AAA. In this model, Ca^{2+} influx causes myosin activation and sliding leading to deformed CSK which is relies on viscoelastic properties regulated by α -actinin2 crosslinking. Using this model (Figure 4a, b; Materials and Methods), we predict that VSMC mechanosensitivity, as defined by the response time to mechanical stimulus, and the ability to generate instantaneous force is directly regulated by the viscoelasticity property of CSK as indicated by expression of α -actinin2 (Figure 4c) and the opening of mechanosensitive ion channel as indicated by the mechanosensitive-induced Ca^{2+} influx (Figure 4d). Our theoretical model thus captured similar VSMC trend (Figure 4e) as our experimental results associating increase α -actinin2 and red shift in CSK tension frequency spectrum in AAA (Figure 3f, 3h). By directly adapting parameters from the mechanobiological ground states of VSMC in AAA and previous experimental studies (Supplementary Table1), our analytical results qualitatively predicted CSK actomyosin dynamics regarding instantaneous CSK tension frequency spectrum (Figure 4f) and force generation (Figure 4g, h) in response to mechanical stimulation. Successful simulation of the instantaneous mechanosensation using the biophysical model underscored the critical role of α -actinin2 in regulating VSMC viscoelastic properties.

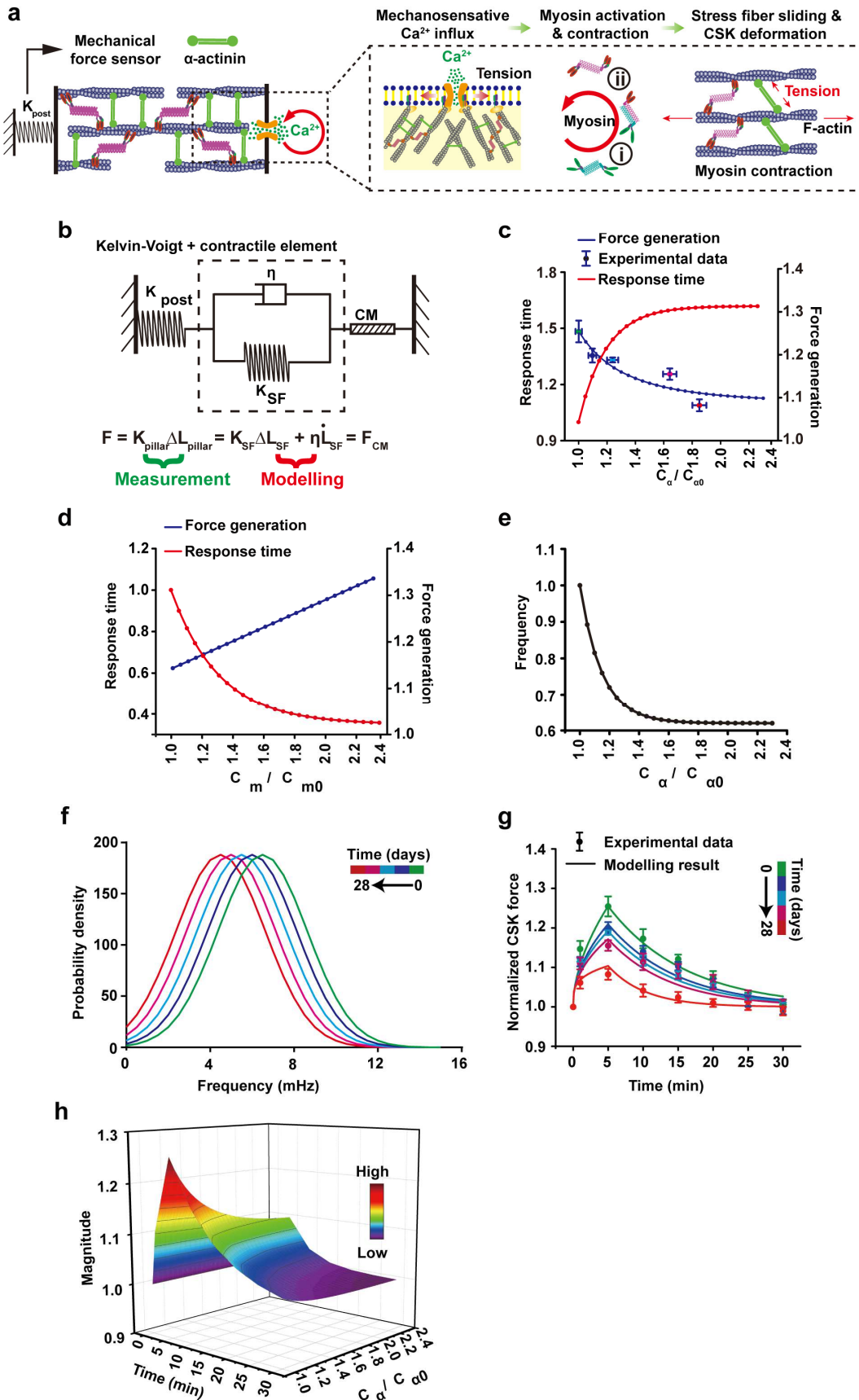


Figure 4. (a) Illustration of the theoretical modelling of VSMC mechanosensation involving three key mechanisms: mechanosensitive Ca^{2+} flux, two-step myosin motor activation and contraction, and stress fiber sliding and CSK deformation. (b) Schematic of VSMC mechanosensation modelled by Kelvin-Voigt element connected in series to the contractile myosin element. (c-d) Force generation ability and response time for VSMC with different expression of α -actinin2 ($C_{\alpha}/C_{\alpha 0}$) (c) and activation of myosin (C_m/C_{m0}) (d) in response to ultrasound tweezer stimulus. (e) Predicted instantaneous central frequency of VSMC mechanosensation with increase of α -actinin2 ($C_{\alpha}/C_{\alpha 0}$). (f) Theoretical prediction of instantaneous frequency distributions of VSMC instantaneous mechanosensation. (g) Alignment of theoretical prediction (solid curves) and experimental measurements (dots with error bar) of force generation dynamics of VSMC instantaneous mechanosensation. (h) Summary three-dimensional plots of the predicted force generation dynamics in mechanosensation of VSMC with different expression of α -actinin2. Experiment data was replotted from Figure 3d. n=8 and data error bars represent s.e.m.

Netrin-1 regulates VSMC stiffness and mechanosensation via α -actinin2

Since our model accurately predicted that increased CSK stiffness driven by α -actinin2 is critical to elevate VSMC mechanosensitivity in AAA, we further investigated the upstream mechanisms triggering the induction of α -actinin2 in VSMC. RNA sequencing (RNAseq) analysis of aorta isolated from aneurysmal WT mice and non-aneurysmal mice with specific Netrin-1 deficiency in macrophages (NKO) subjected to Ang II revealed a library of differentially expressed genes (Figure 5a, left), amongst which the gene encoding Actn2 was the most downregulated transcript in NKO aorta compared to WT controls (Figure 5a, right), suggesting that Netrin-1 could directly regulate the transcription of Actn2 mRNA in the aortic tissue. Immunofluorescence staining of WT aortic sections demonstrated an elevated presence of α -actinin2 in VSMC compared to WT mice treated with PBS (Figure 5b). Analysis of sections from NKO mice treated with Ang II that did not develop AAA, revealed a reduction of α -actinin2 in medial VSMC. These results instructed us that Netrin-1 could regulate α -actinin2 both transcriptionally and translationally in VSMC.

To directly demonstrate whether Netrin-1 could regulate α -actinin2 in VSMC, we performed Western Blot analysis which demonstrated that treatment of VSMC with recombinant Netrin-1 dose dependently increased the expression of α -actinin2 up to 3-fold (Figure 5c). Since our CSK tension model predicted that Actn2 expression would lead to increased tension, we assessed the impact of Netrin-1 stimulation on VSMC membrane force. Consistent with increased α -actinin2 expression, Netrin-1 dose-dependently increased VSMC membrane stiffness by decreasing membrane fluidity of VSMC (Figure 5d). To gain further insights into how Netrin-1 regulates α -actinin2 in VSMC, we treated VSMC with Ca^{2+} chelator, 1,2-bis(o-aminophenoxy) ethane-N,N,N',N'-tetraacetic acid (BAPTA), or Ca^{2+} -sensitive nuclear factor of activated T-cells cytoplasmic 3 (NFATc3)

inhibitor, MAGPHPVIVITGPHEE (VIVIT) peptide, based on our previous data demonstrating that Netrin-1 could activate NFATc3 via Ca^{2+} ²². Western blot analysis showed that treatment of VSMC with BAPTA or VIVIT inhibited Netrin-1-induced expression of α -actinin2 (Figure 5e). VSMC stiffness induced by Netrin-1 was mitigated in the presence of BAPTA, VIVIT or α -actinin2 inhibitor, phosphatidylinositol (3,4,5)-trisphosphate (PtdIns(3,4,5)P3) (Figure 5f). Altogether these results suggested that AAA-promoting signals such as Netrin-1, could regulate VSMC membrane stiffness by stimulating actin fiber crosslinking via α -actinin2.

To test whether aberrant cytoskeletal stress observed in VSMC isolated from AAA could be recapitulated by sustained exposure of recombinant Netrin-1 *in vitro*, we monitored biomechanical and mechanosensation responses of VSMC exposed to Netrin-1 for 1 day. Analysis of images captured by fluorescent microscopy revealed an elevated presence of F-actin stress fibers coincident with α -actinin2 in VSMC exposed to Netrin-1 (Figure 5g). Accordingly, exposure of VSMC to recombinant Netrin-1 increased CSK tension of VSMC captured by micropillar assay (Figure 5h) corollary to VSMC isolated from AAA milieu. Quantification of force per pillar showed a time-dependent increase of CSK tension in VSMC treated with recombinant Netrin-1 (Figure 5i). A similar pattern was observed with VSMC isolated from AAA over the course of disease development (Figure 5j). This is indicative that Netrin-1 can directly coordinate microskeletal stiffness which results in the ablation of VSMC cell membrane fluidity. In-depth force analysis by AFM demonstrated increased expression of α -actinin2 coincident with peaked force intensities in aortic segments of WT mice that developed AAA. In contrast, the overall force of tissue and α -actinin2 expression were reduced in smooth muscle cells harbored in NKO aortas (Figure 5k). Accordingly, PWV demonstrated that the stiffness of NKO aorta was significantly reduced compared to WT mice that developed AAA (Figure 5l). Altogether, these results indicated that VSMC niched in AAA milieu are subjected to abnormal cytoskeletal stress, unlike VSMC that comprise a healthy vascular wall environment. Therefore, our data imply that enhanced CSK tension of VSMC could have a causative role in the pathology of AAA.

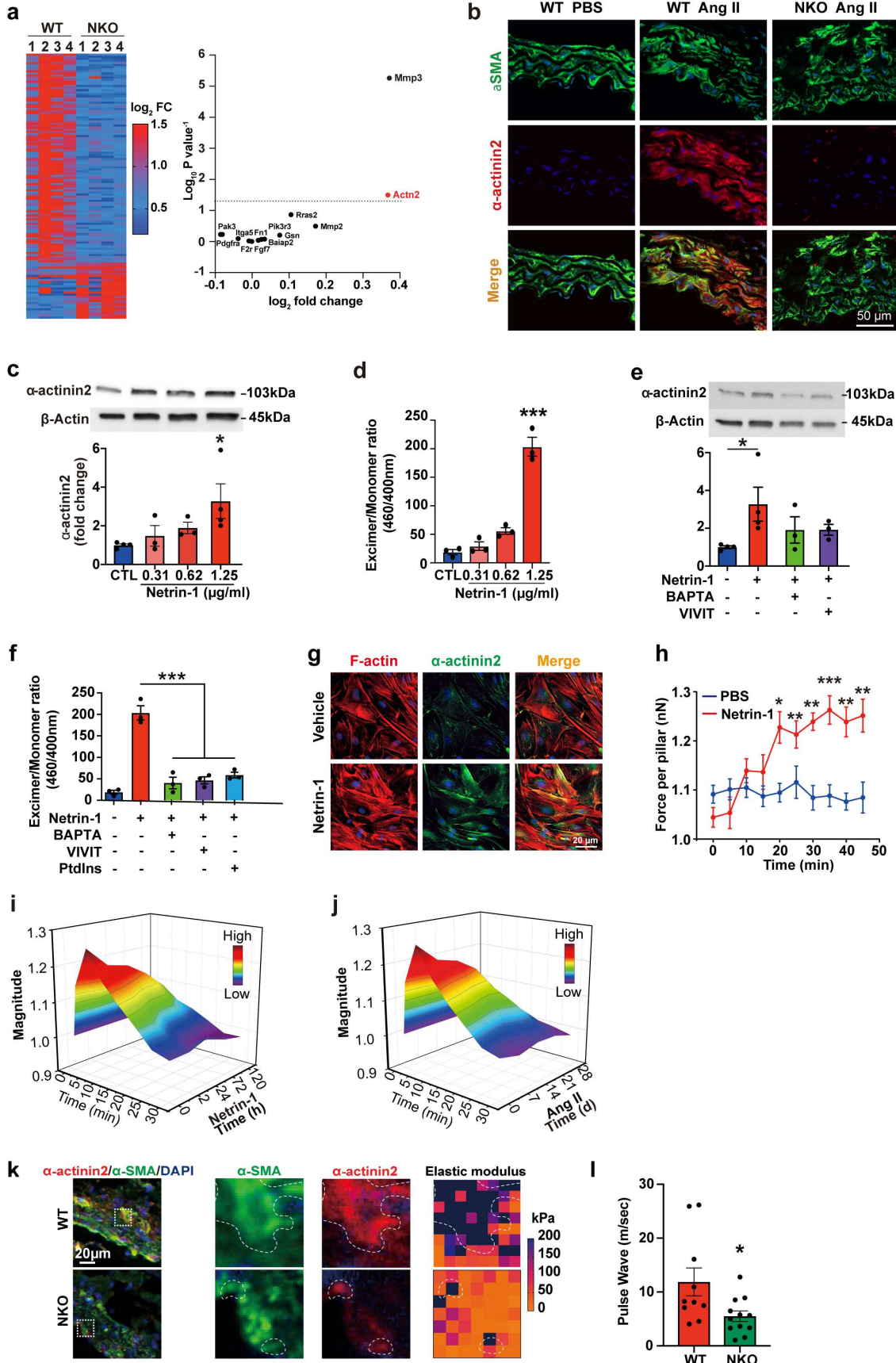


Figure 5. **(a)** Heatmap (left) and dotplot representation (right) of differentially expressed mRNAs associated with CSK regulation in wild type (WT) mice or conditional deficiency of Netrin-1 (NKO) mice perfused with Ang II. FC, fold change. $n= 4$ per group. **(b)** Immunofluorescence (IF) staining of α -actinin2 (red) and α -SMA (green) in aortic sections of WT and NKO mice treated as indicated. **(c)** Immunoblot of α -actinin2 and β -actin expression in VSMC stimulated with recombinant Netrin-1 for 6 hours and quantification of bands. $n= 3$. **(d)** Effects of Netrin-1 or PBS stimulations on VSMC membrane fluidity. Data are expressed as 460/400 nm excimer/monomer ratio. $n=3$. **(e)** Immunoblot of α -actinin2 and β -actin expression in VSMC stimulated with Netrin-1 ($1.25\mu\text{g}/\text{ml}$) or vehicle for 6 hours with or without BAPTA ($1\mu\text{M}$) or VIVIT ($10\mu\text{M}$) and quantification of bands. $n \geq 3$ per group. **(f)** Membrane fluidity of VSMC treated with Netrin-1 in conditions as in **(e)**. $n=3$ per group. **(g)** Representative IF images of α -actinin2 (green) and F-actin (red) in VSMC stimulated with Netrin-1 for 24 hours. $n= 10$ per group. **(h)** Force per pillar measurements at indicated time of VSMC stimulated with Netrin-1 or with PBS. $n \geq 7$. Representative heatmap profiles of traction force distribution in VSMC stimulated with Netrin-1 at indicated timepoints **(i)** and of VSMC isolated from AAA aorta **(j)**. IF staining of α -SMA (green) and α -actinin2 (red) of aortic sections from WT or NKO mice treated with Ang II. Dashed boxes show magnified areas of staining and of AFM depicted by heatmap of elastic modulus force magnitudes (dotted lines show regions of enriched staining and force). **(l)** Aortic pulse wave velocity quantification in WT or NKO mice perfused with Ang II. $n= 10-12$ per group. Nuclei in DAPI (blue) shown in all IF images. Data are represented as mean \pm s.e.m. * $P < 0.05$, *** $P < 0.001$. P values were calculated using one-way ANOVA (c-f) or two-tailed unpaired *t*-test (l).

Mechanosensory ion channel Piezo1 in VSMC in AAA

Since our experimental and theoretical models confirmed a rigidified state of VSMC in AAA, we further investigated the downstream molecular signals triggered by elevated α -actinin2. We first screened for mechanosensory signatures in VSMC by single-cell RNAseq of control and AAA aortas. Since we have previously demonstrated that Netrin-1 regulates Ca^{2+} flux in VSMC²², we focused on profiling mechanosensitive Ca^{2+} ion channels in our dataset. Interestingly, genes encoding for mechanosensitive ion channels with high affinity for Ca^{2+} , Piezo1 and Piezo2 were enriched in AAA tissues (Figure 6a). Quantitative RT-PCR analysis confirmed Piezo1 mRNA was increased by 10-fold in AAA aortas compared to non-diseased control tissues (Figure 6b). No significant difference in Piezo2 was observed in AAA compared to non-diseased aorta. A similar pattern of expression was observed in human specimens of AAA and control aortic tissue revealing increased expression of Piezo1, but not Piezo2 mRNA in diseased samples (Figure 6c). Profiling of Piezo1 in cellular clusters revealed that its expression was concentrated in VSMC in AAA (Figure 6d, e). Immunofluorescence staining confirmed that Piezo1 protein levels were increased in AAA and co-localized with α -SMA positive VSMC (Figure 6f). Furthermore, Piezo1 protein expression was increased time-dependently in VSMC

isolated from aortas of mice with early, middle and advanced stages of AAA development (Figure 6g). Altogether, these findings indicate that Piezo1 is a novel downstream mechano-effector of Netrin-1 in AAA.

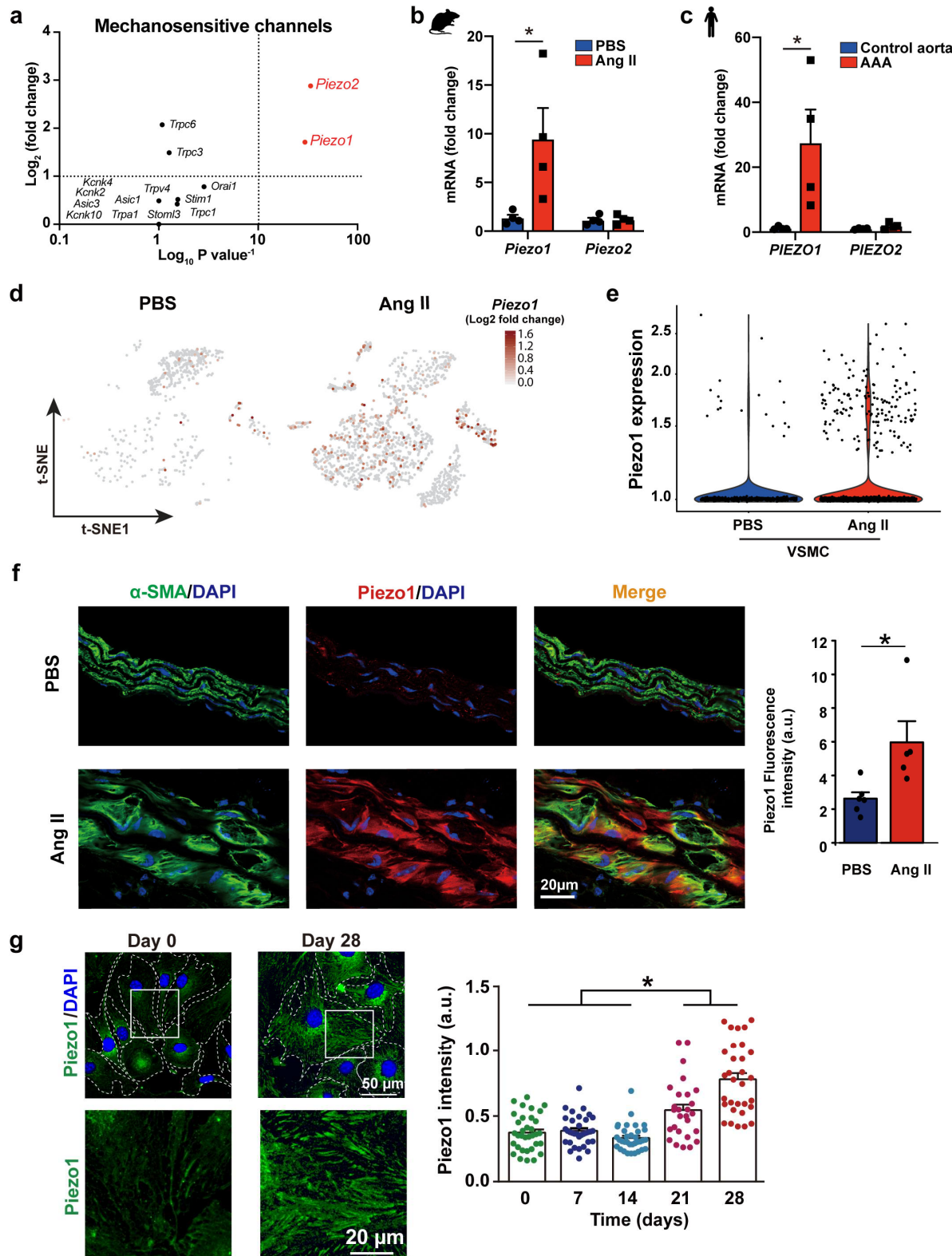


Figure 6. (a) Dotplot representation showing differential expression (\log_2) and P value of mechanosensitive channel transcripts in AAA compared to control aortas. Quantitative-RT-PCR (qPCR) analysis of *Piezo1* and *Piezo2* mRNA levels in aorta of mice treated with PBS or Ang II (b) or *PIEZO1* and *PIEZO2* transcripts in healthy or AAA human aortic specimens (c). n=4 per group. (d) *Piezo1* mRNA levels and distribution within cell clusters in single cell RNAseq of aortas from mice perfused with Ang II or PBS, and violin plot representation of *Piezo1* expression in VSMC (e). (f) Representative IF microscopy image of *Piezo1* (red) and α -SMA (green) staining in aorta of mice as indicated and quantification. n= 5 per group. a.u., arbitrary unit. (g) IF staining of *Piezo1* and quantification of intensity in VSMC isolated from aorta of mice perfused with Ang II for 0 (control) or 28 days. n \geq 27. Nuclei in DAPI (blue) shown in all IF images. Data are represented as mean \pm s.e.m. *P < 0.05. P values were calculated using two-tailed unpaired t-test (b,c,f) or one-way ANOVA (g).

Netrin-1 regulates intracellular Ca^{2+} influx via *Piezo1* in VSMC

We further evaluated the functional significance of elevated *Piezo1* induced by Netrin-1 in VSMC. Microscopy images showed that stimulation of VSMC with Yoda1, a specific agonist of *Piezo1*^{34,35}, significantly increased intracellular Ca^{2+} influx (Figure 7a) which was maintained for 200 seconds in VSMC (Figure 7b). This was mostly dependent on extracellular pools of Ca^{2+} since Yoda1-induced intracellular flux of Ca^{2+} was abrogated in conditions when the media was depleted of Ca^{2+} (Figure 7a, b). In the presence of GsMTx4 peptide, an antagonist previously shown to block *Piezo1* channels³⁶, the increase of intracellular Ca^{2+} flux induced by Yoda1 was reduced (Figure 7a, c) suggesting that GsMTx4 can block mechano-activation of Ca^{2+} via *Piezo1* in VSMC. Netrin-1 triggered a robust Ca^{2+} influx in VSMC but was mitigated in the presence of GsMTx4 (Figure 7d, e). AFM microscopy revealed that areas enriched with *Piezo1* in aortic sections of AAA thoroughly mapped with territories of increased force magnitudes within the tissue. *Piezo1* expression and force intensity within NKO aortic sections were weaker (Figure 7f). This was consistent with α -actinin2 force patterns observed between WT and NKO sections. Altogether, these findings suggested a central role for Netrin-1 in fueling Ca^{2+} supply to VSMC by mechanically powering *Piezo1* channels.

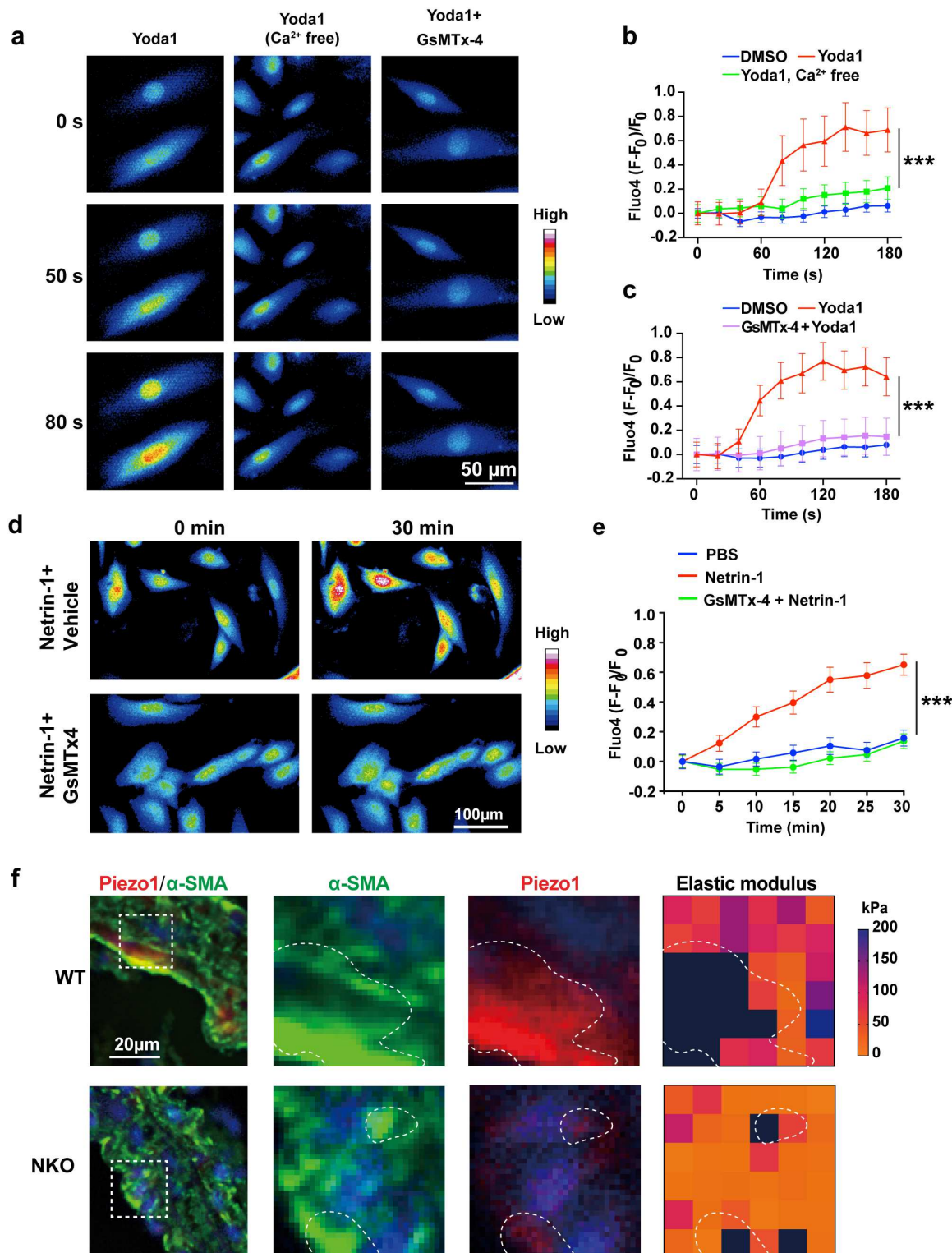


Figure 7. (a) Representative IF images of intracellular Ca²⁺ signal in VSMC treated with reagents and time period as indicated. Signal intensity scale is indicated on the right. (b,c) Time course quantification of Ca²⁺ flux in VSMC treated as indicated. $n \geq 25$ per group. Representative microscopy images (d) and quantification (e) of Ca²⁺ levels in VSMC

treated as indicated for 30 minutes. $n \geq 24$ per group. (f) IF staining of α -SMA (green) and Piezo1 (red) in aortic sections of WT or NKO mice perfused with Ang II. Dashed box indicates magnified area of AFM and immunostaining. Force and Piezo1 with areas of interest are outlined. Nuclei in DAPI (blue). Data are represented as mean \pm s.e.m.; *** P < 0.001. P values were calculated using one-way ANOVA.

Antagonizing Piezo1 prevents AAA development

On the basis of the experimental and theoretic results reported above, we postulated that antagonizing Piezo1 would impede ECM destruction and curb AAA development. We therefore exposed mice to continuous subcutaneous infusion of Ang II and subjected them to vehicle or GsMTx4 treatment (Figure 8a). The incidence of AAA was decreased with GsMTx4 treatment consistent with reduced disease severity (Figure 8b, c). Doppler ultrasound images captured enlarged aorta in vehicle-treated mice, but not in those exposed to GsMTx4 (Figure 8d, top). Quantification of maximum aortic diameter confirmed that Ang II treatment increased aortic dilatation, which was reduced in the presence of GsMTx4 (Figure 8d, bottom). These results suggested that negatively interfering with Piezo1 activation rescued mice from developing AAA. We previously demonstrated that Netrin-1 commands the release of proteolytic enzyme, MMP3, by VSMC to drive elastin degradation in AAA²². To investigate whether MMP3 is downstream of Piezo1 activation in VSMC, we first profiled MMP3 expression in our single cell RNAseq analysis. Results demonstrate that MMP3 was enriched in VSMC populations in AAA (Figure 8e, f). Stimulation of VSMC with recombinant Netrin-1 induced MMP3 activity which was blunted in the presence of GsMTx4 validating that Netrin-1 regulates MMP3 via Piezo1 in VSMC (Figure 8g). Immunofluorescence staining confirmed the reduced expression of MMP3 in VSMC in aortic section of mice treated with GsMTx4 compared to controls (Figure 8h). This was consistent with reduced elastin fiber damage characterized by thicker and unfragmented fibers, in vascular wall of mice treated with GsMTx4 in accordance with non-diseased phenotype (Figure 8i). Together, these results invoke that suppressing Piezo1-mediated mechanotransduction hinders proteolytic damage of the aorta and is likely to decelerate AAA growth in patients should such drug-based approach be brought to the clinical setting.

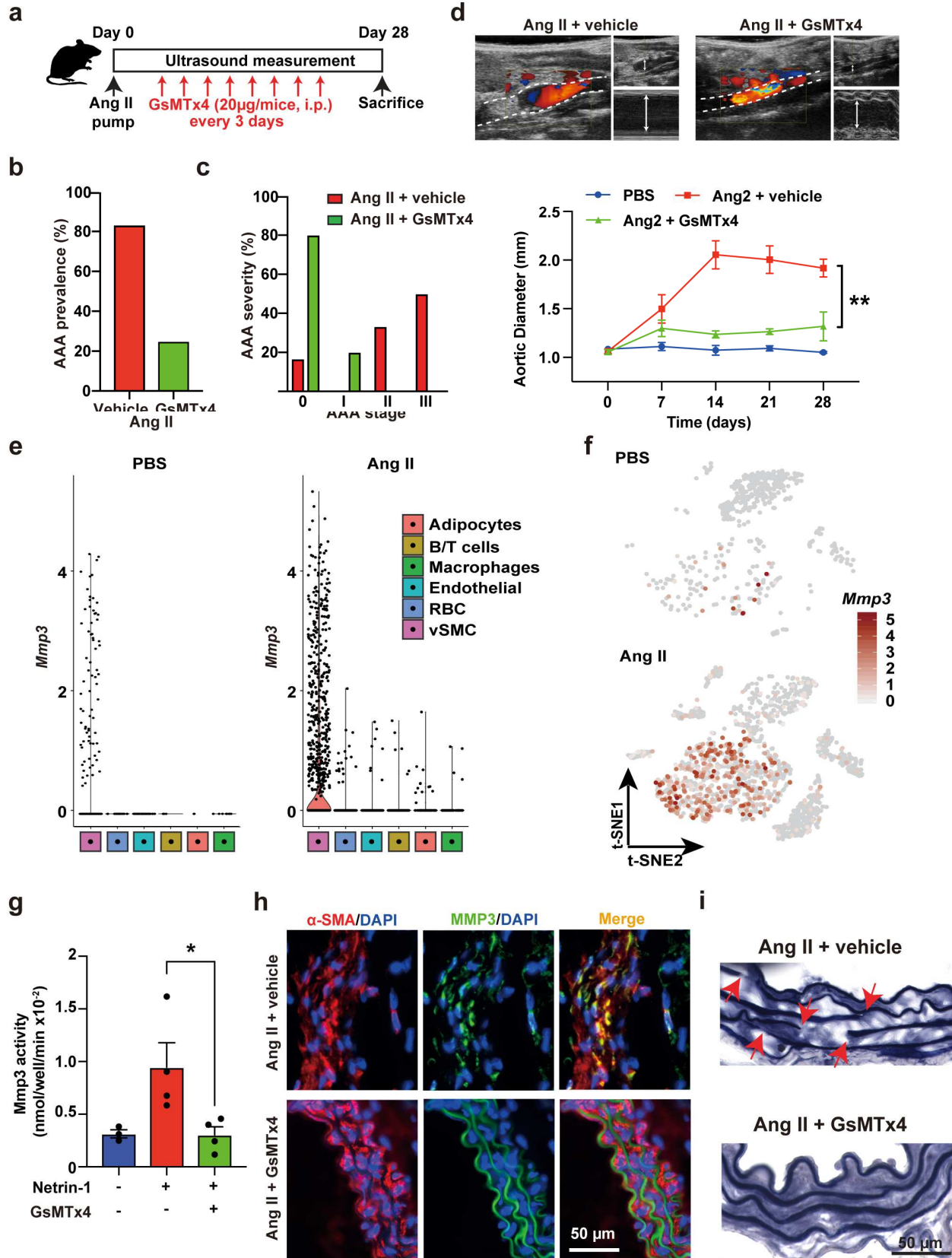


Figure 8. (a) Schematic representation of GsMTx4 treatment during AAA induction. i.p., intraperitoneal. AAA prevalence (b) and AAA severity score (c) in mice perfused with Ang II with or without GsMTx4. (d) Representative color Doppler ultrasound images (upper panels) of aortic flow and measurements of maximum transverse aortic diameter over time, as indicated, (lower panel). Dotted line delimits aortic wall. Arrows show maximum diameter. $n \geq 4$ per group. Violin plot of Mmp3 mRNA expression per cluster (e) and its t-SNE distribution in single-cell RNA seq dataset of aortas of mice treated with PBS or Ang II. (g) Mmp3 activity assay in VSMC stimulated with Netrin-1 or control, with or without GsMTx4. $n \geq 3$ per group. (h) Immunofluorescence staining of Mmp3 (green) and α -SMA (red) in aortas of mice exposed to Ang II, vehicle or GsMTx4. $n \geq 3$ per group. Nuclei in stained with DAPI (blue). (i) Verhoeff-Van Gieson elastin staining in aortas of mice perfused with Ang II and treated with GsMTx4 or vehicle. Arrows indicate elastin breaking points. $n=3$ per group. Data are represented as mean \pm s.e.m.; * $P < 0.05$, ** $P < 0.01$; P values were calculated by two-tailed unpaired *t*-test (d) or one-way ANOVA (g).

DISCUSSION

In this study, we mapped a novel mechano-molecular trajectory connecting AAA-prone signals that provoke robust response of mechanosensitive ion channel, Piezo1 to fuel matrix degradation during AAA progression (Supplementary figure 5). We observed increased stiffness of the vascular framework in aneurysmal conditions where cellular and extracellular constituents are damaged. This biomechanic pattern was reciprocated in VSMC isolated from AAA aorta or in the presence of AAA-promoting signal Netrin-1. Notably, we demonstrate that pathological mechanical load of VSMC was fueled by increased expression of CSK crosslinker, α -actinin2, thereby mitigating intracellular mechanotransduction signals and powering the opening of Piezo1 channels. These results are consistent with other studies that have demonstrated elevated stiffness and dysfunctional mechanosensing in aneurysmal aortic tissue^{37,38,39}. Our findings extend on this knowledge by invoking that VSMC are instrumental bearers of defective mechanosensing during AAA and identify Piezo1 as a novel causative target to curb AAA.

It is unsurprising that epidemiologic studies have established associations between increased stiffness and AAA^{37,40} given that AAA affects almost exclusively the aged population (≥ 65 years) and that stiffness of the aorta culminates with aging^{41,42}. Further comprehensive studies have dissected that increased mechanical stress not only positively correlated with risk of rupture⁴³ but also coincided with the rate of expansion of AAA⁴⁴. These clinical findings were recapitulated in experimental AAA modeled by elastase infusion which demonstrated that elevated segmental aortic stiffening could be a stimulus that initiates AAA growth. Our findings of increased stiffness are consistent with the latter study, although we used experimental AAA modeled by Ang II infusion. This suggests that elevated mechanical load is an overlapping feature between these two experimental models and is an intrinsic trait of AAA.

In contrast to the extensive study of unicellular “static” biophysical properties and their relation to cell status, exploring how cells dynamically respond to cellular architecture and pathological mechanical stimuli has been a challenge especially in cells that are embedded in pulsatile tissues such as the aorta. We engineered a sophisticated micromechanical system to bypass these challenges by allowing the monitoring of time-variant molecular activities and CSK dynamics in response to transient perturbations of VSMC. Using an ultrasound tweezers-based integrative micromechanical system, we revealed both the progressive and instantaneous mechanosensation behaviors of VSMC to transient mechanical stimulus. We show that compromised mechanosensation of VSMC is acquired gradually as AAA develops. Similar mechanic allosteric shifts were observed in non-pathological VSMC treated with Netrin-1. This adds on to our previous studies demonstrating that mechanical perturbations are integrators that determine distinct mechanophenotypes in diseases^{29,30}. Such changes in mechanosensation of VSMC can be attributable to the overexpression of α -actinin2 which causes a more solid-like property of CSK. Moreover, AFM revealed that VSMC within AAA tissue are stiff and PWV validated increased aortic tissue stiffness consistent with results obtained with our micromechanical system. Our results indicate that measuring VSMC mechanosensation behaviors might be used a new biophysical marker to evaluate AAA progression. Combined with theoretically modelling, our analysis of VSMC mechanosensation can provide insights into the pathological molecular machinery that drives the compromised force generation ability of VSMC in AAA and may help to provide guidelines in selecting pharmaceutical candidates for inhibiting AAA.

Our results demonstrate that in advanced stages of AAA, the accumulation of secreted molecules such as Netrin-1 provoked the increase of VSMC tension by finetuning actin fiber crosslinking through α -actinin2, thereby powering Piezo1 activation in VSMC. This is consistent with other studies that demonstrated that Netrin-1 regulated macrophage motility⁴⁵ and neuron outgrowth⁴⁶ by modulating actin filament machinery though FAK activation. We therefore demonstrate a novel concept illustrating that non-mechanical stimulus (secreted Netrin-1) can coordinate with increased cellular tension to activate the expression and responsiveness of Piezo1 in VSMC. We also demonstrate that Piezo1 is transcriptionally regulated in tensed VSMC and AAA tissue. This most likely reflects a feed-forward mechanism initiated by increased vascular tension and Netrin-1 that sustains transcriptional regulation of the gene encoding for Piezo1⁴⁷. Importantly, this suggests that in homeostasis conditions, VSMC niched within complex mechanically active microenvironments and subjected to concentric pressure load, the expression of Piezo1 is repressed basally to avoid overactivation of Ca^{2+} signals. Indeed, we observed that Piezo1 was weakly expressed at baseline in VSMC within non-diseased aortic tissue. This feedback regulatory mechanism seems to be compromised with the surge of Netrin-1 stemming from arterial macrophages in the microenvironment of VSMC thereby promoting AAA.

Therefore, breaking this pathological circuitry by targeting Piezo1 is a highly

desirable goal as it would allow the elimination of signals that promote a continuum in matrix degradation permissive to AAA development. We show that treatment of mice prone to develop AAA with GsMTx4 prevented AAA incidence by refraining the influx of Ca^{2+} in VSMC. Our *in vitro* studies show that Netrin-1-induced Ca^{2+} influx and MMP3 activity can be repressed in the presence of GsMTx4. Notably, evidence suggests that treatment of patients undergoing endovascular repair to prevent AAA rupture, with a Ca^{2+} channel blocker, demonstrated beneficial outcomes on the repair intervention as evaluated by AAA sac shrinkage⁴⁸. Our results show that targeting upstream importer of Ca^{2+} that are selectively upregulated during disease development in VSMC could provide a more specific target in refraining exaggerated matrix degrading enzyme activation in AAA.

Taken together, our study provides sophisticated models that revealed novel insights into the mechanism of Piezo1 mediated pathological mechanosensation in AAA. We speculate that artificially predicting mechanical behaviors of cells within AAA combined with targeting Piezo1 could be promising strategies to develop in the scope of limiting AAA growth.

MATERIALS & METHODS

Mice

Mice used in our experiments, including C57BL/6J (WT), LysMcre and ApoE^{-/-} mice were bought from Jackson Laboratories. Ntn1^{flox/flox}LysMcre^{+/−} and control Ntn1^{flox/flox} mice were generated as described previously²². Mice were bred in a pathogen-free facility and provided a standard chow diet unless otherwise stated. In each experiment group, mice were randomly distributed, and no predetermination of sample size was conducted by statistical method. The US Department of Agriculture Animal Welfare Act, the Public Health Service Policy for the Humane Care and Use of Laboratory Animals and the New York University School of Medicine's Institutional Animal Care and Use Committee approved all experimental procedures which were conducted according to their guidelines.

AAA induction in mice

Procedures described previously²² were used to induce AAA in mice. Briefly, 8-week old male ApoE^{-/-} mice were implanted with Alzet osmotic pumps (#2004; Durect Corporation) sub-cutaneously for a continuous 28-day delivery of PBS (control) or angiotensin II (H-1705, Bachem) at 1 µg/kg/min. For Ntn1^{flox/flox}LysMcre^{+/−} and Ntn1^{flox/flox} littermates on C57BL/6J background, AAA was induced by increasing their cholesterol through exposure of adeno-associated virus vector (AAV) overexpressing proprotein convertase subtilisin/kexin type 9 (PCSK9) by intraperitoneal injections contiguous with a Western diet (WD; 21% [wt/wt] fat, 0.3% cholesterol; Research Diets) feeding for 2 weeks prior to osmotic pump implantation. Mice developed AAA when maintained on Western diet throughout angiotensin II perfusion as described previously⁴⁹. For piezo1 inhibition experiments, ApoE^{-/-} mice received intraperitoneal injections of GsMTx4 (STG-100, Alomone Labs), 20µg/mice every 3 days. Severity of AAA was evaluated at sacrifice based gross morphological aortic alterations as per guidelines⁵⁰.

Human samples

New York University Langone Medical Center Institutional Review Board approved this study upon informed consent from each human subject that underwent open aortic surgery. Non-pathological aortas from certified brain-dead organ donors provided by the LiveOnNY organization (NY, New York) were used as controls. Samples were divided into pieces for sectioning or frozen for molecular analysis.

Cell culture

Mouse primary VSMC were isolated from control and aneurysmal aortas that were freshly dissected. Adventitial fat was carefully removed from the dissected aortas, minced into pieces and processed for digestion for 10 min at 37 °C in an enzymatic mix composed of type II collagenase (10 mg/ml, C6885, Sigma Aldrich) and elastase (1 mg/ml, LS002292, Worthington Biochemistry). The samples were further digested for 50 minutes in the

enzymatic mix after removal of adventitia under a dissecting microscope. Single cell suspensions were obtained after passage of digested lysate through a 70 µm cell-strainer. Cells were grown in DMEM supplemented by 10% fetal bovine serum and 1% penicillin-streptomycin until confluence and used for assays as outlined in the manuscript. VSMC purity was verified by content of alpha-actin by flow cytometry.

Western blotting

Protein content of samples were collected in RIPA buffer (98065; Cell Signaling Technologies) and loaded onto a 10% Mini-PROTEAN TGX gel (#456-8034, Bio-Rad) for SDS-PAGE and transferred to PVDF membranes (#BR20160719, Bio-Rad) using a Trans-Blot Turbo Transfer System (Bio-Rad). Non-specific signals were blocked and membranes were probed using anti- α -actinin2 (1:500 dilution; 14221-1-AP, Proteintech) and anti- α -actin (sc-130656, Santa Cruz Biotechnology) antibodies. HRP conjugated secondary antibodies, goat anti-rabbit (1:5000 dilution; 7074P2, Cell Signaling) or goat anti-mouse (1:5000 dilution; A9917, Sigma Aldrich) were incubated with the membranes. Protein bands were revealed by applying Clarity Western ECL (#170-5060, Bio-Rad) and imaged on a ChemiDoc Imaging System (Bio-Rad). Mean band intensities were quantified with ImageJ and α -actinin2 levels were determined in samples by normalization to control.

Membrane rigidity assay

Membrane rigidity was assessed using the Membrane fluidity kit (ab189819, Abcam) as per manufacturer's instruction. Mouse VSMC were seeded in flat bottom clear 96 well plates (5.10^4 cells/well). Cells were stimulated for 24 hours with recombinant Netrin-1 (1109-N1, R&D Systems) in the presence or absence of VIVIT peptide (MAGPHPVIVITGPHEE peptide, #3905, Tocris Biosciences, 1µM), BAPTA (B1205, Invitrogen, 10µM) or PtdIns-(3,4,5)-P3 (10007764, Cayman Chemical, 25µM). All pharmacological inhibitors were added 1 hour before Netrin-1 stimulation. Following treatment, cells were washed and stained for 20 minutes at 37°C, 5% CO₂, using the 10µM Fluorescent Lipid Reading containing 0.08% Pluronic F127 in perfusion buffer, all provided in the kit. Cells were then washed twice and fluorescence was measured immediately using a FlexStation 3® Multi-Mode Microplate Reader (Molecular Devices). Fluorescence was measured at 400 and 460nm and data expressed as the ratio of values captured at 460 nm and 400 nm wavelengths.

RNA sequencing

RNA sequencing of WT and NKO bulk abdominal aortic tissues were performed as described previously²². Only samples of optimal RNA quality were run on a HiSeq (Illumina) using single-end reads. FASTQ files were aligned to the MM9 Mus musculus reference genome using Tophat (version 2.0.9). Differential gene expression analysis was

performed using the DESEQ2 package from Bioconductor running on R statistical program. For single cell RNA sequencing, control and AAA aortas were digested in a single suspension as described above and loaded on a 10x Genomics Chromium instrument to obtain individual gel beads in emulsion (GEMs). Chromium Single Cell 3' Library & Gel Bead Kit v2, PN-120237, the Single Cell 3' Chip Kit v2 PN-120236 and the i7 Multiplex Kit PN-120262, (10x Genomics) were used for library preparation. Illumina HiSeq 4000 as 2 x 150 paired-end reads was used for sequencing (>90% sequencing saturation). Cell Ranger Single Cell Software Suite, version 1.3, was used to perform demultiplexing, barcode and UMI processing, and single-cell 3' gene counting (<https://support.10xgenomics.com/single-cell-gene>). Data analysis was performed using the 'Seurat' version 3.1.2 package, using R Studio Desktop, version 1.2.5033, and R, version R 3.0.1+. Quality control, metrics, data normalization, scaling and dimension reductions were all performed using the Seurat package. Cells with mitochondrial transcript proportion <5% were kept for analysis, neighboring and clustering was performed on the most significant principle component analysis using a 0.5 resolution. The VSMC cluster, identified based on the enrichment in *Acta2* and *Myh11* specific markers, was used for differential expression in the control and AAA group. P values were adjusted using the Benjamini-Hochberg method for false discovery correction. Genes with an adjusted P value < 0.05 were considered as differentially expressed and used for Gene Set Enrichment Analyses (GSEA) using the DAVID online open resource. All scripts are available from authors upon reasonable request.

Real-time quantitative PCR

Aortic samples were lysed in TRIzol (15596026, Ambion, Life Technologies) and RNA isolation was performed using the Directzol RNA MiniPrep Kit (R2052, Zymo Research). Following reverse transcription using the cDNA Synthesis Kit (1708890, Bio-Rad), quantitative real-time PCR was performed with KAPA SYBR FAST qPCR Kits (KK4602, KAPA Biosystems) using a QuantStudio 3 Real-Time PCR System (Applied Biosystems). The primer sequence set used were:

muPiezo1:Forward: GCTCTTAACCATTGAGCCATCT, Reverse: GCCTAGATTCACCTGGCTTC; muPiezo2: Forward: CTCAGCCATTTAGCCTTGC, Reverse: CAGATCCTTGCGTCTCTCC; huPiezo1: Forward: CAATGAGGAGGCCGACTACC, Reverse: GCACTCCTGCAGTCGATGA; huPiezo2: Forward: GCCCAACAAAGCCAGTTGAA, Reverse: GGGCTGATGGTCCACAAAGA; 28S: Forward: TGGAATGCAGCCCCAAG, Reverse: CCTTACGGTACTTGTGACTATCG.

Fold change differences were calculated after normalization to housekeeping gene by the comparative cycle method ($2^{-\Delta\Delta Ct}$).

Immunofluorescence staining and microscopy

Sectioning of frozen murine aortic samples conserved in Optimal Cutting Temperature

Compound (OCT; 4585, Fisher Scientific) generated 7- μ m-thick sections which were fixed in 10% formalin buffer prior for immunostaining. Sections prepared in paraffin were deparaffinized, processed for tissue rehydration and antigen retrieval using EDTA and Tween solution as previously described²². VSMC were fixed in 4% paraformaldehyde (Electron Microscopy Sciences) for 30 min and then permeabilized with 0.3% Triton X-100 (Roche Applied Science) for 10 min at room temperature. Staining was performed by applying overnight incubation of primary antibodies: anti- α -actinin2 (#14221-1-AP, Proteintech), anti-Piezo1, (#15939-1-AP, Proteintech), or anti-alpha-smooth muscle actin (#48938S, Cell Signaling) (1:200 dilution each). Alexa Fluor 488 and 647 conjugated anti-IgG antibodies (Invitrogen) were used for fluorescent signal detection. Alexa Fluor 555 conjugated to phalloidin (Invitrogen) and 4',6-diamidino-2-phenylindole (DAPI; Invitrogen) were used for visualization of actin microfilaments and nucleus respectively. Images were acquired using a Zeiss LSM 710 confocal microscope (Carl Zeiss) through the Zeiss Efficient Navigation (ZEN) software (Carl Zeiss). Identical acquisition parameters were set to capture control and test samples. Learning Unsupervised Means of Spectra (LUMoS)⁵¹ method (ImageJ) was used for analysis of staining intensity of some markers of VSMC.

Atomic force microscopy (AFM)

Aortic samples were cryosectioned using Leica CM3050S cryostat and immobilized to glass-bottom dish (WPI's FluoroDish™) precoated with poly-D-Lysine for 24 hours. An MFP-3D-BIO Atomic Force Microscope (Asylum Research, Oxford Instruments, Santa Barbara, CA) was used to obtain force maps from different locations of aortic tissues. A 6.1 μ m spherical polystyrene bead AFM probe (CP CONT-PS-C, NanoAndMore Lady's Island, SC) was used for all indentation measurements. The actual spring constant was 0.27N/m. The calibration of Z-distance deflection and the cantilever stiffness was determined by InvOLS and thermal tune calibration was determined following previous protocols⁵². The force-distance used was 8 μ m with a scan rate of 1Hz and the trigger point was customized at 5 nN. The force-indentation curves were fit to the Hertz model⁵³ for spherical tips utilizing the Asylum Research Software to determine the Young's Modulus, with an assumed Poisson's ratio value of 0.45 for the sample. The stiffness determined for the Young's Modulus values on each point force measured of the grid were then exported from the Asylum Research Software for further analysis. An inverted microscope (Zeiss Axio Observer Z1) was used to acquire brightfield images of the aortic tissues to localize the region for the stiffness measurements.

Traction force measurement using micropillar array

VSMC CSK contractility was measured using previously described micropillar array⁵⁴. Micropillar array was fabricated through a two-time molding. A silicon master mold with micropillar of ~7 μ m height was first fabricated by standard photolithography and deep reactive ion etching (DRIE). A negative PDMS mold was constructed by mixing 1:10 ratio

PDMS prepolymer to the silicon mold and baked at 110 °C for 30 mins. The negative PDMS mold was peeled off the silicon mold and silanized with tridecafluoro-1,1,2,2, -tetrahydrooctyl)-1-trichlorosilane (Sigma-Aldrich) overnight in vacuum. To generate the PDMS micropillar array, a drop of 1:10 ratio PDMS was added to the silanized PDMS negative mold and covered with oxygen plasma (350W, PlasmaEtch) treated cover glass. The “Cover glass-PDMS-negative mold” sandwich structure was cured in an oven heated at 110°C. Cover glass with PDMS micropillar array was peeled off from negative mould and sonicated in 100% ethanol to restore collapsed micropillar. The array was dried and mounted on a petri dish with a 13 mm hole at the bottom. Prior to CSK contractility measurements, the micropillar was primed with fibronectin (50 µg/ml; Sigma-Aldrich) and Alexa-Fluor 647-conjugated fibrinogen (25 µg/ml; Life Technologies) by microcontact printing so as to label the tip of pillar necessary for imaging as previously shown⁵⁵. VSMC were cultured on the micropillar array overnight prior to mechanical stimulation and analysis. CSK contractility was analyzed by quantifying the deflection of micropillar using the Cellogram⁵⁶ and custom-developed MATLAB programs (Mathworks).

Scanning electron microscopy (SEM)

VSMCs were cultured on micropillar overnight. The samples were then washed three times with 50 mM Na-cacodylate buffer (pH 7.3; Sigma-Aldrich) and fixed for 1 hr with 2% glutaraldehyde (Electron Microscopy Sciences) in 50 mM Na-cacodylate buffer. Fixed samples were dehydrated using a graded series of ethonal concentrations. Basically, samples were first immersed in 30%, 50%, 70%, 80%, and 90% of ethonal for 10 mins, respectively, and then dehydrated in 100% of ethanol three times, each time for 20 mins. The dehydrated samples were dried using a super critical point dryer (Samdri®-PVT-3D, Tousimis) according to the instruction of manufacturer. To perform SEM, dried samples were mounted on stubs and sputtered with gold palladium for 15 s, observed and imaged under a Hitachi S-3400N Ultra-High Resolution SEM machine (Hitachi High Technologies America).

Mechanical stimulation of VSMC

Mechanical stimulation using ultrasound tweezers for VSMC instantaneous mechanosensation was performed as previously described^{28,29}. VSMC were functionalized with Targestar™-SA lipid microbubbles from Targeson (San Diego, CA) through RGD-integrin-CSK linkage. To functionalize microbubble surface with RGD peptide 1 µL of microbubbles solution ($3 \times 10^9/\text{mL}$) was mixed with 4 µL of biotinylated Arg-Gly-Asp (RGD) peptide (2 mg/mL, Peptides International) for 20 min at room temperature. Cell culture medium was removed from VSMC dish and replaced with 30 µL of the diluted microbubble-RGD added to the center of the micropillar array. The micropillar array was then flipped over in a cell culture incubator for 10 min to allow binding of microbubbles to VSMC. Unbound microbubbles were washed away with cell culture medium. VSMC attached to microbubbles were used for ultrasound tweezers stimulation.

To generate ultrasound pulses for stretching microbubble, a 10-MHz ultrasound transducer (V312-SM, Olympus) was used and driven by a function generator (Agilent Technologies 33250A) and a 75 W power amplifier (Amplifier Research 75A250). The ultrasound transducer was then calibrated and fixed at a 45° angle to the cell surface plane. The distance between the transducer and VSMC was calibrated to be 11.25 mm (Rayleigh distance) by using an Olympus pulser receiver. Ultrasound pulse was applied at a frequency of 1 Hz for 10s on each VSMC with microbubble attached. Deflection of the micropillar array underneath VSMC was continuously imaged to record the dynamics of CSK contractility and quantified as described above.

Spectral analysis of VSMC force dynamics

To perform spectral analysis of VSMC force dynamics, the quantified VSMC real-time CSK contractility was sampled upon discretized windows which was generated by a previously developed algorithm³¹. We subsequently sampled time series of local force dynamics on each window to analyze localized force fluctuation. Based on the Empirical mode decomposition (EMD) of Hilbert-Huang transform^{57,58}, we decompose the localized force dynamics into several analytical elementary signals, so called as intrinsic mode functions (IMFs). We then computed the instantaneous frequency spectra through Hilbert transform for all IMFs in all sampled windows, with central frequency hierarchically spanning from high to low values corresponding to IMF1-5. We also computed the frequency weighted quadratic amplitude of all IMFs to reflect the instantaneous energy consumed by the entire cell³¹. The temporal force response ratio is defined as $1 - e^{t/T_c}$ where T_c is the characteristic adaptation time that is equal to the reciprocal of IMF central frequency³².

Biophysical modeling of VSMC instantaneouse mechanosensation

In the KVM model, the Kelvin-Voigt element, which is the cell CSK is modelled as a viscoelastic material consisting of elastic stress fiber (SF) with an elastic module of K_{SF} and a viscous component with viscosity of η . The contractile myosin (CM) element is modelled in series configuration with the viscoelastic CSK structure^{33,59}. The elastic module of K_{SF} is proportional to the amount of α-actinin2 and is described as $k_{sf}C_\alpha$, where C_α represents the amount of α-actinin2 for a VSMC; k_{sf} is a scaling factor. To specifically study the change of VMSC CSK tension arising from contraction of myosin, we modelled the KVM configuration in series so that the change in CSK tension is equal to the change of myosin contraction upon mechanical input. The KVM configuration can be further connected to an elastic substrate, which is the micropillar array (K_{pillar}) used to experimentally measure the change of CSK tension during the instantaneous mechanosensation process. As the KMV configuration is modelled in series, the Kelvin-Voigt element and the contractile myosin share the same tension, which is equal to the measured mechanical force by micropillar array,

$$F = K_{pillar}\Delta L_{pillar} = K_{SF}\Delta L_{SF} + \eta\dot{L}_{SF} = F_{CM} \quad (1)$$

where for L_{SF} , the dot indicates the time derivative as required for calculating stress of a viscoelastic material; F_{CM} is the contractile force due to the sliding of activated myosin depending on the deformation of the CSK. To investigate the effect of change in CSK properties, herein the elevated expression of α -actinin2 in VSMC during AAA development, we modelled the F_{CM} as an instantaneous mechanical actuator that deforms CSK. The dynamic deformation and relaxation of CSK reflects dynamic accumulation and decay of mechanical tension. Therefore, the modelled VSMC mechanosensation dynamics are directly related to the mechanically activated Ca^{2+} influx induced by myosin contraction and CSK behavior. To determine the magnitude of the mechanical actuator that deforms CSK, F_{CM} was modelled to be directly proportional to the activated myosin ($C_{m,max}$), which is related to Ca^{2+} influx upon mechanical stimulus. However, not all activated myosin contributed to the deformation of CSK. Therefore, $F_{CM} \propto k_m C_{m,max}$, where $C_{m,max}$ is the maximum amount of activated myosin ; k_m is a scaling constant. As we didn't see obvious differences of change of maximum Ca^{2+} influx upon mechanical stimulus for VSMC isolated from mice at different stages of AAA, $C_{m,max}$ was kept constant. The Kelvin-Voigt element represents the viscoelastic property of CSK and is directly related to the expression of α -actinin2 in our model. Upon an application of instantaneous mechanical force by contractile myosin, we modelled the deformation of CSK to closely follow a power law over time with an exponent β that reflects the viscoelasticity of CSK, $\Delta L_{SF} \propto t^\beta$. The deformation is also related to the magnitude of CSK tension by activated myosin, hence $\Delta L_{SF} = k_m C_{m,max} t^\beta$. A material with a larger β indicates more viscous and smaller β indicates more elastic. We can then express β as $k_\beta \frac{\eta}{K_{SF}}$, where k_β is a scaling factor. At the same time, more expression of α -actinin2 indicates a more elastic material and $\beta = \frac{k_{\beta,a}}{c_\alpha}$, where $k_{\beta,a}$ is a scaling factor. Hence, we can model the tension accumulation in CSK upon deformation,

$$F = K_{SF} \Delta L_{SF} + \eta \dot{L}_{SF} = k_{sf} C_\alpha k_m C_{m,max} \left(t^{\frac{k_{\beta,a}}{c_\alpha}} + \left(\frac{k_{\beta,a}}{c_\alpha} \right)^2 t^{\left(\frac{k_{\beta,a}}{c_\alpha} - 1 \right)} \right) \quad (2)$$

According to our experimental mechanosensation dynamics analysis, after $t_1 = 5$ minutes of continuous accumulation of CSK tension, the CSK start to relax which should follow the relaxation of a Kelvin-Voigt material,

$$F = k_{sf} C_\alpha k_m C_{m,max} \left(t_1^{\frac{k_{\beta,a}}{c_\alpha}} + \left(\frac{k_{\beta,a}}{c_\alpha} \right)^2 t_1^{\left(\frac{k_{\beta,a}}{c_\alpha} - 1 \right)} \right) (e^{-(t-t_1)\frac{k_{rex}}{\beta}}) \quad (3)$$

where k_{rex} is the scaling factor for the exponential relaxation event.

To model the temporal propagation of probability density function (PDF) associated with the instantaneous frequency distribution, We employ Fokker-Planck equation³²:

$$\frac{\partial p(\omega, t)}{\partial t} = \frac{\partial (\omega - \omega_c) p(\omega, t)}{\partial \omega} + D \frac{\partial^2 p(\omega, t)}{\partial \omega^2}$$

$$\omega_c = \sqrt{\frac{K_{SF}}{(C_\alpha V_\alpha M_\alpha + C_m V_m M_m)} - \left(\frac{\eta}{2(C_\alpha V_\alpha M_\alpha + C_m V_m M_m)} \right)^2}$$

Where $p(\omega, t)$ is the temporal PDF of instantaneous angular frequency, $\omega_c = 2\pi f_c$ is the central angular frequency that represents the overall spectral response of the VSMC, and D represents the magnitude of environmental noise that diverges the central frequency. In the expression of central angular frequency ω_c , V_α and V_m are the volume of α -actinin2 and myosin solution, while M_α and M_m are the molecular weight of α -actinin2 and myosin molecules. Taking the stationary solution of the above partial differential equation:

$$p(\omega) = \frac{1}{\sqrt{2\pi D}} e^{-\frac{(\omega-\omega_c)^2}{2D}}$$

By fitting the modeling PDF curves to the experimental frequency histograms of different cell conditions, we find a good agreement between the theoretical prediction and experimental results, indicating a loss of mechanosensation upon the cellular force generation.

Calcium imaging

Mice primary VSMC seeded on micropillar array were washed twice using normal physiological saline solution (NPSS) with 140 mM sodium chloride, 5 mM potassium chloride, 2 mM magnesium chloride, 1 mM calcium chloride, 10 mM HEPES, and 10 mM glucose. Cells were then loaded for 20 mins with calcium probe Fluo-4 (F14201, Thermo Fisher Scientific) followed by two washes with NPSS. Imaging was performed using a Zeiss Axio observer with a 20X objective excited at 480nm. Before recording data, Ca^{2+} signal was stabilized by imaging VSMC continuously every 1 second for 6 minutes. To image Ca^{2+} in VSMC upon mechanical stimulation, VSMC were imaged every 200 ms and mechanical stimulation was applied 3 seconds from the start of the recording. To image Ca^{2+} in VSMC with drug stimulation, Yoda1 (#21904, Cayman Chemical) or recombinant mouse Netrin-1 (#1109-N1, R&D Systems) at a final concentration of 30 μM and 2.5 $\mu\text{g/ml}$ were respectively added to VSMC media. For Piezo1 inhibition assays, cells were preincubated with 2.5 μM GsMTx4 (#STG-100, Alomone labs) for 10 min prior to stimulation.

Statistical analysis

All data were from at least three independent experiments, and presented as means \pm s.e.m. The means of groups were compared using one-way analysis of variance (ANOVA) followed by Tukey's post hoc test in GraphPad Prism or unpaired, two-tailed Student's t-test in Excel (Microsoft), as shown in figure captions. P-value smaller than 0.05 was considered statistically significant.

Data availability

All data associated with this study are present in the paper and Supplementary Information. The authors declare that all data supporting the results in this study are available within the paper and its Supplementary Information. Raw data are available from the corresponding author on reasonable request.

Acknowledgements

We acknowledge financial support from the American Heart Association Scientist Development Grant (16SDG31020038) and the National Institute of Health (R35GM133646) to W.C. Part of the study was funded by National Institute of Health (R01 HL146627) to B.R.

Author contributions

B.R., W.C. conceptually developed and supervised the project and designed experiments. B.R., W.C. wrote the manuscript assisted by W.Q. and T.H. W.Q, T.H., C.F.R., A.B., M.S., B.M., Z.Z., H.Q., and B.B. performed experiments; W.Q, T.H, X.M. and W.C. analyzed data. A.C. help with graphical illustration. A.B., G.M. provided feedback and discussion.

COMPETING FINANCIAL INTERESTS

The authors declare no competing financial interest.

References

1. Kent, K.C. Abdominal Aortic Aneurysms. *New England Journal of Medicine* **371**, 2101-2108 (2014).
2. Sampson, U.K., et al. Estimation of global and regional incidence and prevalence of abdominal aortic aneurysms 1990 to 2010. *Global heart* **9**, 159-170 (2014).
3. Raffort, J., et al. Monocytes and macrophages in abdominal aortic aneurysm. *Nature Reviews Cardiology* **14**, 457-471 (2017).
4. Hellenthal, F.A.M.V.I., Buurman, W.A., Wodzig, W.K.W.H. & Schurink, G.W.H. Biomarkers of AAA progression. Part 1: extracellular matrix degeneration. *Nature Reviews Cardiology* **6**, 464-474 (2009).
5. Milewicz, D.M., et al. Altered smooth muscle cell force generation as a driver of thoracic aortic aneurysms and dissections. *Arterioscler Thromb Vasc Biol* **37**, 26-34 (2017).
6. Weng, S., Shao, Y., Chen, W. & Fu, J. Mechanosensitive subcellular rheostasis drives emergent single-cell mechanical homeostasis. *Nature materials* **15**, 961-967 (2016).
7. Anwar, M., Shalhoub, J., Lim, C., Gohel, M. & Davies, A. The effect of pressure-induced mechanical stretch on vascular wall differential gene expression. *Journal of vascular research* **49**, 463-478 (2012).
8. Martinez-Quinones, P., et al. Hypertension induced morphological and physiological changes in cells of the arterial wall. *American journal of hypertension* **31**, 1067-1078 (2018).
9. Brown, I.A., et al. Vascular smooth muscle remodeling in conductive and resistance arteries in hypertension. *Arterioscler Thromb Vasc Biol* **38**, 1969-1985 (2018).
10. Kim, T.-J., et al. Distinct mechanisms regulating mechanical force-induced Ca²⁺ signals at the plasma membrane and the ER in human MSCs. *eLife* **4**, e04876 (2015).
11. Ribeiro, C.M.P., Reece, J. & Putney, J.W. Role of the cytoskeleton in calcium signaling in NIH 3T3 cells An intact cytoskeleton is required for agonist-induced [Ca²⁺] i signaling, but not for capacitative calcium entry. *Journal of Biological Chemistry* **272**, 26555-26561 (1997).
12. Alenghat, F.J., Nauli, S.M., Kolb, R., Zhou, J. & Ingber, D.E. Global cytoskeletal control of mechanotransduction in kidney epithelial cells. *Experimental cell research* **301**, 23-30 (2004).
13. Coste, B., et al. Piezo1 and Piezo2 Are Essential Components of Distinct Mechanically Activated Cation Channels. *Science* **330**, 55 (2010).
14. Coste, B., et al. Piezo proteins are pore-forming subunits of mechanically activated channels. *Nature* **483**, 176-181 (2012).
15. Cox, C.D., et al. Removal of the mechanoprotective influence of the cytoskeleton reveals PIEZO1 is gated by bilayer tension. *Nature Communications* **7**, 10366 (2016).
16. Romac, J.M.J., Shahid, R.A., Swain, S.M., Vigna, S.R. & Liddle, R.A. Piezo1 is a mechanically activated ion channel and mediates pressure induced pancreatitis. *Nature Communications* **9**, 1715 (2018).
17. Chen, X., et al. A Feedforward Mechanism Mediated by Mechanosensitive Ion Channel PIEZO1 and Tissue Mechanics Promotes Glioma Aggression. *Neuron* **100**, 799-815.e797 (2018).
18. Li, J., et al. Piezo1 integration of vascular architecture with physiological force. *Nature* **515**,

- 279-282 (2014).
- 19. Ranade, S.S., et al. Piezo1, a mechanically activated ion channel, is required for vascular development in mice. *Proceedings of the National Academy of Sciences* **111**, 10347-10352 (2014).
 - 20. Retailleau, K., et al. Piezo1 in Smooth Muscle Cells Is Involved in Hypertension-Dependent Arterial Remodeling. *Cell Reports* **13**, 1161-1171 (2015).
 - 21. Alebrahim, D., et al. Mapping Semaphorins and Netrins in the Pathogenesis of Human Thoracic Aortic Aneurysms. *International journal of molecular sciences* **20**, 2100 (2019).
 - 22. Hadi, T., et al. Macrophage-derived netrin-1 promotes abdominal aortic aneurysm formation by activating MMP3 in vascular smooth muscle cells. *Nature Communications* **9**, 5022 (2018).
 - 23. van Gils, J.M., et al. The neuroimmune guidance cue netrin-1 promotes atherosclerosis by inhibiting the emigration of macrophages from plaques. *Nature Immunology* **13**, 136-143 (2012).
 - 24. Di Lascio, N., Kusmic, C., Stea, F. & Faita, F. Ultrasound-based Pulse Wave Velocity Evaluation in Mice. *J Vis Exp* (2017).
 - 25. Lu, Q., Jiang, X., Zhang, C., Zhang, W. & Zhang, W. Noninvasive Regional Aortic Stiffness for Monitoring the Early Stage of Abdominal Aortic Aneurysm in Mice. *Heart Lung Circ* **26**, 395-403 (2017).
 - 26. Murphy, A.C.H. & Young, P.W. The actinin family of actin cross-linking proteins – a genetic perspective. *Cell & Bioscience* **5**, 49 (2015).
 - 27. Ribeiro Ede, A., Jr., et al. The structure and regulation of human muscle alpha-actinin. *Cell* **159**, 1447-1460 (2014).
 - 28. Fan, Z., et al. Acoustic tweezing cytometry for live-cell subcellular modulation of intracellular cytoskeleton contractility. *Scientific Reports* **3**, 2176 (2013).
 - 29. Wang, Q., et al. Energy-Mediated Machinery Drives Cellular Mechanical Allostasis. *Advanced Materials* **31**, 1900453 (2019).
 - 30. Qian, W. & Chen, W. Probing Single-Cell Mechanical Allostasis Using Ultrasound Tweezers. *Cellular and Molecular Bioengineering* **12**, 415-427 (2019).
 - 31. Ma, X., Dagliyan, O., Hahn, K.M. & Danuser, G. Profiling cellular morphodynamics by spatiotemporal spectrum decomposition. *PLOS Computational Biology* **14**, e1006321 (2018).
 - 32. Cohen, O. & Safran, S.A. Theory of frequency response of mechanically driven cardiomyocytes. *Scientific reports* **8**, 1-8 (2018).
 - 33. Wu, T. & Feng, James J. A Biomechanical Model for Fluidization of Cells under Dynamic Strain. *Biophys J* **108**, 43-52 (2015).
 - 34. Syeda, R., et al. Chemical activation of the mechanotransduction channel Piezo1. *Elife* **4**, e07369 (2015).
 - 35. Lacroix, J.J., Botello-Smith, W.M. & Luo, Y. Probing the gating mechanism of the mechanosensitive channel Piezo1 with the small molecule Yoda1. *Nature communications* **9**, 1-13 (2018).
 - 36. Bae, C., Sachs, F. & Gottlieb, P.A. The mechanosensitive ion channel Piezo1 is inhibited by the peptide GsMTx4. *Biochemistry* **50**, 6295-6300 (2011).

37. He, C.M. & Roach, M.R. The composition and mechanical properties of abdominal aortic aneurysms. *Journal of Vascular Surgery* **20**, 6-13 (1994).
38. Humphrey, J.D., Milewicz, D.M., Tellides, G. & Schwartz, M.A. Cell biology. Dysfunctional mechanosensing in aneurysms. *Science* **344**, 477-479 (2014).
39. Li, Z.Y., et al. Association between aneurysm shoulder stress and abdominal aortic aneurysm expansion: a longitudinal follow-up study. *Circulation* **122**, 1815-1822 (2010).
40. Vande Geest, J.P., Sacks, M.S. & Vorp, D.A. The effects of aneurysm on the biaxial mechanical behavior of human abdominal aorta. *Journal of Biomechanics* **39**, 1324-1334 (2006).
41. Mitchell, G.F., et al. Changes in arterial stiffness and wave reflection with advancing age in healthy men and women: the Framingham Heart Study. *Hypertension* **43**, 1239-1245 (2004).
42. Safar, M.E. Arterial aging--hemodynamic changes and therapeutic options. *Nat Rev Cardiol* **7**, 442-449 (2010).
43. Fillinger, M.F., Marra, S.P., Raghavan, M.L. & Kennedy, F.E. Prediction of rupture risk in abdominal aortic aneurysm during observation: wall stress versus diameter. *J Vasc Surg* **37**, 724-732 (2003).
44. Li, Z.-Y., et al. Association Between Aneurysm Shoulder Stress and Abdominal Aortic Aneurysm Expansion. *Circulation* **122**, 1815-1822 (2010).
45. van Gils, J.M., et al. The neuroimmune guidance cue netrin-1 promotes atherosclerosis by inhibiting the emigration of macrophages from plaques. *Nat Immunol* **13**, 136-143 (2012).
46. Ren, X.R., et al. Focal adhesion kinase in netrin-1 signaling. *Nat Neurosci* **7**, 1204-1212 (2004).
47. Chen, X., et al. A Feedforward Mechanism Mediated by Mechanosensitive Ion Channel PIEZO1 and Tissue Mechanics Promotes Glioma Aggression. *Neuron* **100**, 799-815 e797 (2018).
48. Bailey, M.A., et al. Calcium channel blockers enhance sac shrinkage after endovascular aneurysm repair. *J Vasc Surg* **55**, 1593-1599 (2012).
49. Lu, H., et al. Hypercholesterolemia Induced by a PCSK9 Gain-of-Function Mutation Augments Angiotensin II-Induced Abdominal Aortic Aneurysms in C57BL/6 Mice—Brief Report. *Arterioscler Thromb Vasc Biol* **36**, 1753-1757 (2016).
50. Manning, M.W., Cassis, L.A., Huang, J., Szilvassy, S.J. & Daugherty, A. Abdominal aortic aneurysms: fresh insights from a novel animal model of the disease. *Vascular Medicine* **7**, 45-54 (2002).
51. McRae, T.D., Oleksyn, D., Miller, J. & Gao, Y.R. Robust blind spectral unmixing for fluorescence microscopy using unsupervised learning. *PLoS One* **14**, e0225410 (2019).
52. Zoellner, H., Paknejad, N., Manova, K. & Moore, M.A. A novel cell-stiffness-fingerprinting analysis by scanning atomic force microscopy: comparison of fibroblasts and diverse cancer cell lines. *Histochem Cell Biol* **144**, 533-542 (2015).
53. Wang, B., et al. A general approach for the microrheology of cancer cells by atomic force microscopy. *Micron* **44**, 287-297 (2013).
54. Fu, J., et al. Mechanical regulation of cell function with geometrically modulated elastomeric

- substrates. *Nature Methods* **7**, 733-736 (2010).
- 55. Alom Ruiz, S. & Chen, C.S. Microcontact printing: A tool to pattern. *Soft Matter* **3**, 168-177 (2007).
 - 56. Lendenmann, T., et al. Cellogram: On-the-Fly Traction Force Microscopy. *Nano Letters* **19**, 6742-6750 (2019).
 - 57. Huang, N.E., et al. The empirical mode decomposition and the Hilbert spectrum for nonlinear and non-stationary time series analysis. *Proceedings of the Royal Society of London. Series A: mathematical, physical and engineering sciences* **454**, 903-995 (1998).
 - 58. Huang, N.E., et al. A confidence limit for the empirical mode decomposition and Hilbert spectral analysis. *Proceedings of the Royal Society of London. Series A: Mathematical, Physical and Engineering Sciences* **459**, 2317-2345 (2003).
 - 59. Besser, A. & Schwarz, U.S. Coupling biochemistry and mechanics in cell adhesion: a model for inhomogeneous stress fiber contraction. *New Journal of Physics* **9**, 425 (2007).

Supplementary Files

This is a list of supplementary files associated with this preprint. Click to download.

- [Microskeletalstiffnesssupplementaryinfo.pdf](#)